Chapter 5

Wide field imaging

"If you have built castles in the air,
your work need not be lost;
that is where they should be.
Now put the foundations under them."
- H. D. Thoreau

In this chapter, we discuss the synthesis and analysis of wide field dirty images from MRT. We start with a simple procedure to correct for the errors in time stamping the data files. We then describe a few aspects of the calibration technique used and discuss the amplitude and phase stability of the array. Aspects of the wide field imaging with the non-coplanar MRT, including the limitations of Tangent Plane Approximation (TPA) for inversion of visibilities and the imaging carried out by the method of Fourier phasing are presented. We discuss the problems due to differential precession in combining images made with different allocations from visibilities observed over a large period of time (about five years). Analysis of each allocation's image to check its quality like rms noise in the image, detection of well known point sources, effect of correlator offsets and estimation of relative gains to co-add the images made on different days are discussed. Preliminary investigations of full resolution dirty images obtained are also presented.

5.1 Timing errors

During the observations carried out in the second cycle (for block-3 (172 m-261 m) and block-4 (262 m-351 m); Sec. 2.1.1), the sidereal clock used for time stamping the data was set[1] incorrectly from the true time due to which the time stamped in the data file is 54.1 seconds less than the true sidereal time. This error has been taken care of at various stages of data processing.

The sidereal time is stamped at the end of each integration period. Only the hour, minute and seconds (only the integer part) part of the sidereal time are recorded in the data file (i.e. only up to nearest preceding second). At the start of observations, it is ensured that the fractional part of the true sidereal time (expressed in sidereal seconds) is close to zero. But, due to hardware latency between the astronomical clock and the actual start of the observations there is an offset of less than one sidereal second. Due to this offset the actual observations start slightly later and the fractional part of the true sidereal time (expressed in sidereal seconds) at the start is equal to this offset.

In view of this, there is an uncertainty up to 1 sidereal second in the time stamped in the data file which results in inaccuracies during calibration and further processing. We developed a technique to correct for the errors in time stamping to improve the accuracy with which the sidereal time of the observed visibilities can be estimated. It uses the fact that the integration time of the visibilities is known to an accuracy better than $1\mu s$ and the timing information available from the astronomical clock is accurate down to a reso-

[1]This was due to an error in the program used to convert the local time to sidereal time. So although the sidereal clock was set almost everyday, it was offset during the second cycle of observation in these two blocks. This has been corrected for all observations during the third cycle.

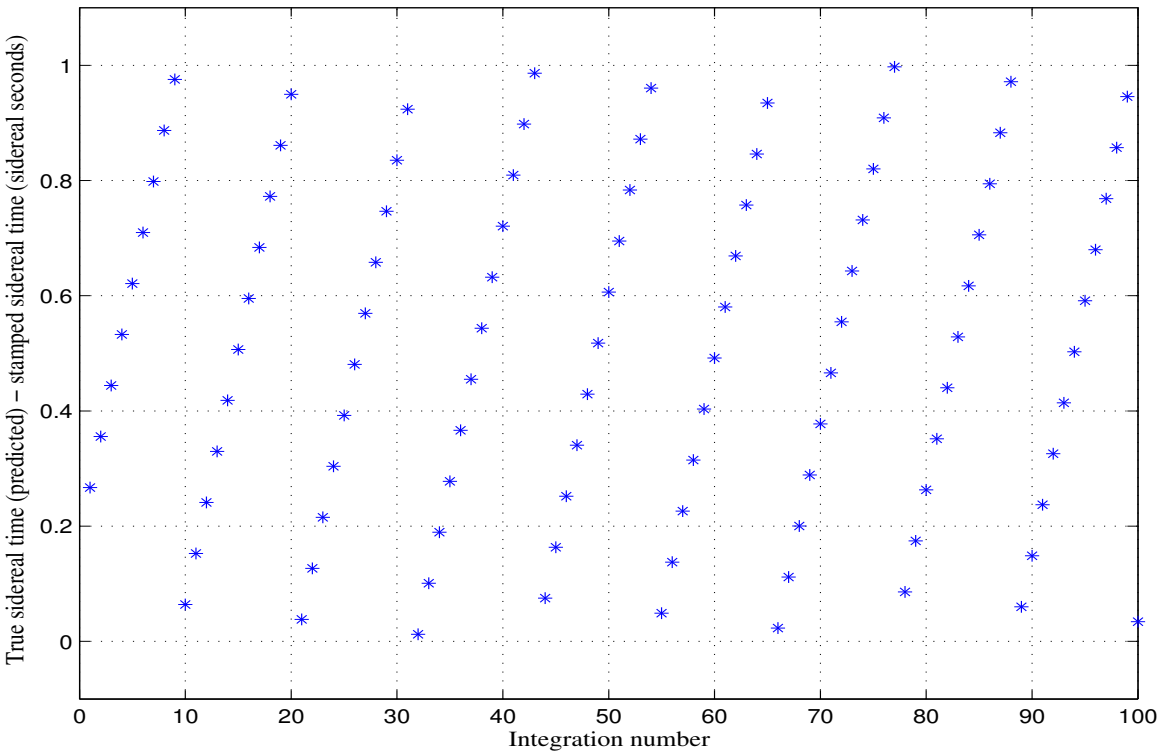

Fig. 5.1: Difference between the true sidereal time (predicted) and the sidereal time stamped in the data file for the first 100 integration periods of a visibility file. The difference as seen is simply the fractional part of the true sidereal time (expressed in sidereal seconds) and varies between 0 and 1 sidereal seconds, in a periodic manner every 11-12 integration periods.

lution of 1 millisecond. Using the developed technique, the sidereal time of the observed visibilities can be estimated to an accuracy close to a millisecond.

Let us assume that the sidereal time stamps in a given file are $t_0, t_1, ..., t_{n-1}$ sidereal seconds for each of the integration periods $1, 2, ..., n$. Let the actual offset due to the hardware latency at the start of observation with the sidereal clock be t_e where t_e <1 sidereal second. The true times for the visibilities observed is given by $t_0 + t_e, t_0 + t_e + t_p, ..., t_0 + t_e + (n-1)t_p$, where t_p is the integration time of the visibilities in sidereal seconds. As the time stamped in the data file is recorded only up to the preceding sidereal second, it can also be written as $I(t_0 + t_e), I(t_0 + t_e + t_p), ..., I(t_0 + t_e + (n-1)t_p)$ where I is the integer function which returns only the integer part of its argument. Thus at any instant the difference between the true sidereal time and the stamped sidereal time is simply the fractional part of the true sidereal time expressed in sidereal seconds. At times when this fractional part is zero, the true sidereal time and the stamped sidereal time would be equal. Since the integration period[2] is ≈1.09 s the fractional part (and thus the difference between the true sidereal time and the

[2]The integration period for observations carried out in the first cycle is 1.09525719 s and for the observations during the second and the third cycles it is 1.08855679 s.

stamped sidereal time) would build up and increase for the next 11-12 integration periods, after which it would drop again to a low value. This cycle gets repeated for every 11-12 integration periods in a similar way. Thus, on an average the difference in the true sidereal time and the stamped time would be close to 0.5 s. Fig. 5.1 shows the difference between the true sidereal time (predicted by the developed scheme which is discussed later) and the stamped sidereal time as a function of integration number for the first 100 integration periods of a visibility file. As expected the difference periodically varies between the range 0 to 1 sidereal second. The difference builds up from a low value till it reaches close to 1 s and drops down to a low value (which can be zero also). Now we discuss the method developed to estimate the true sidereal time of the observed visibilities accurately.

In the estimation of the true sidereal time of the observation of the visibilities the only unknown variable is t_e. To get the best possible estimate of the offset t_e, we minimize the function $E(t_e)$ which measures the mean of the absolute difference between the expected sidereal time stamps and the actual sidereal time stamped in the data file as given by the expression,

$$E(t_e) = \frac{1}{n}\sum_{i=1}^{n} abs[I\{t_0 + t_e + (i-1)t_p\} - t_i] \tag{5.1}$$

where *abs* implies the absolute value of its argument. The value of $E(t_e)$ depends upon the assumed value of offset t_e and is minimum when t_e has the value equal to the actual offset. We cannot estimate t_e to an accuracy better than a millisecond as the timing information from the astronomical clock is accurate down to a resolution of 1 millisecond. We vary t_e in steps of 1 millisecond from 0 to 999 milliseconds. The value of t_e which minimizes $E(t_e)$ gives us the required offset using which we can estimate the actual time of the observation of the visibilities, $t_0 + t_e, t_0 + t_e + t_p, ..., t_0 + t_e + (n-1)t_p$.

Data Slips and Glitches :

The above discussion holds true under the assumption that there are no data slips and data glitches during the observation. Data slips occur when the visibilities corresponding to an integration period has been missed in the data file i.e. they have not been recorded in the data file. Data glitch occurs when the visibility corresponding to a particular integration period gets repeated i.e. it is recorded again in the data file. Data slips and glitches can occur due to a variety of reasons like communication errors between hardware, latency etc.. Due to this for accurate estimation of the sidereal time using the procedure described above, we also take into account the data slips and glitches. In addition, there are also occasional errors during the time stamping when some bits get erroneously recorded. Such cases of erroneous recording are rare (one in 100 files) and can generally be easily figured out by simple filtering schemes. Now we describe the practical implementation of

the above scheme.

Practical implementation :

A flow chart depicting the steps involved in the developed scheme to correct for errors in time stamping is shown in the Fig. 5.2. First the outliers i.e. occasional erroneous recorded time stamps are identified and replaced by representative values by passing the entire sequence of time stamps through a Hampel filter. In the next stage, the identification of data slips and data glitches is carried out. Subsequently, the mean absolute difference in the predicted time stamps and the time stamped in the data file is calculated using Eqn. 5.1 for different assumed values of the offset t_e, starting from 0 millisecond up to 999 milliseconds in steps of 1 millisecond. The value of the offset t_e, which gives the minimum value of the mean of absolute difference between the predicted sidereal time stamps and the stamped time in the data file is considered as the actual offset.

This improvement in the estimation of sidereal time of the visibilities is carried out before any other data processing steps are executed. The original data file is not modified at any stage and this accurately estimated sidereal time is stored in a separate file. In subsequent stages of data processing, the programs use this accurate sidereal time (up to $\approx$1 millisecond) instead of the time stamped in the original visibility file. Fig. 5.3 and Fig. 5.4 show the improvement achieved for a visibility file having 3307 integration periods covering observations for one sidereal hour duration. The mean difference between the true sidereal time and the time stamped in the data file is $\approx$0.50 s. When the sidereal time is estimated using the technique described above, the mean difference between the predicted sidereal time stamps and the time stamped in the data file gets reduced to only 0.00064 s. This clearly reveals the accurate estimation of the sidereal time of the recorded visibilities.

In case this minimum value of $E(t_e)$ exceeds a given threshold (one part in forty), the original sidereal time as recorded in the data is used as a precautionary measure. The threshold has been kept in mind after inspecting the time correction results in a few visibility files. The chances of such occurrences are although rare ($\approx$1 in 200 files).

5.2 Calibration of visibilities at MRT

The observed visibility in general is affected by a variety of reasons and is different from the true visibility. The aim of calibration is to recover the true visibility from the measured visibility. In general the relationship between the observed visibility and true visibility can be a complicated one. Fortunately, due to sound engineering practices it is a good approximation to assume the array to be a linear device which ensures a linear relationship

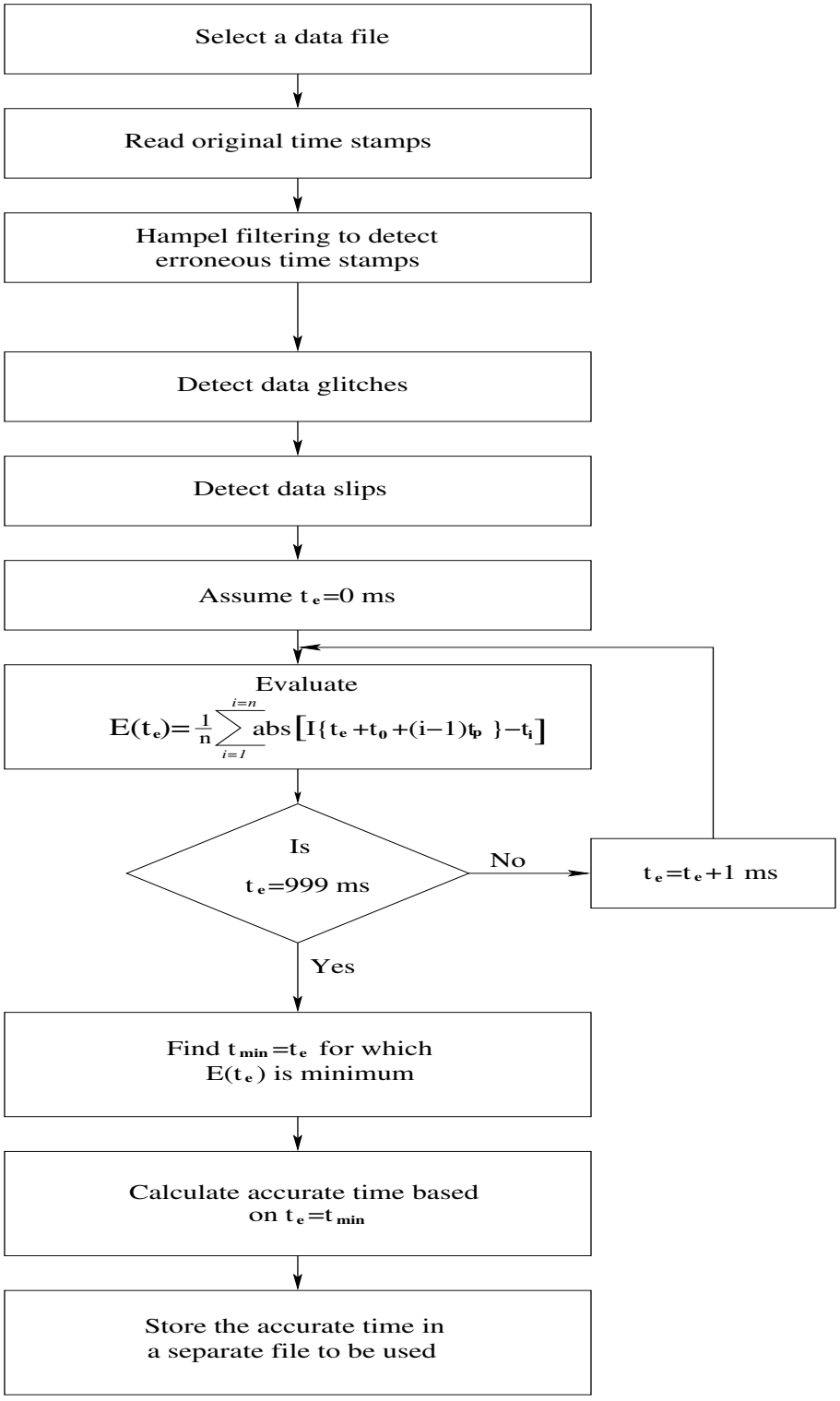

Fig. 5.2: Flow chart showing the steps involved to correct for the errors in time stamping to estimate the sidereal time of the visibilities accurate to 1 millisecond.

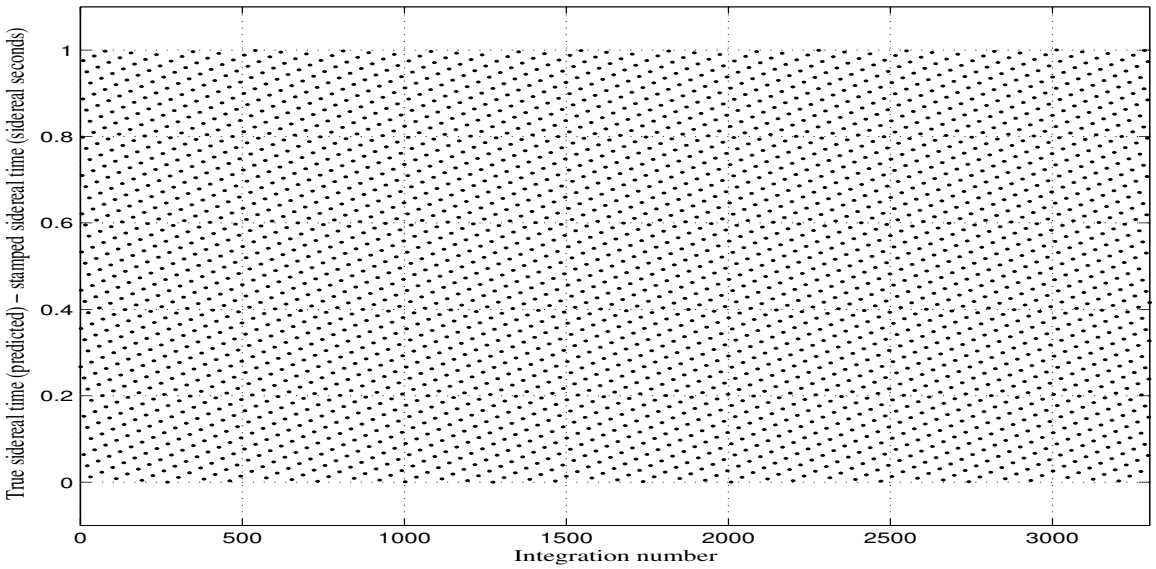

(a) Difference (marked as dots) between the true sidereal time (predicted) and the sidereal time stamped in the data file.

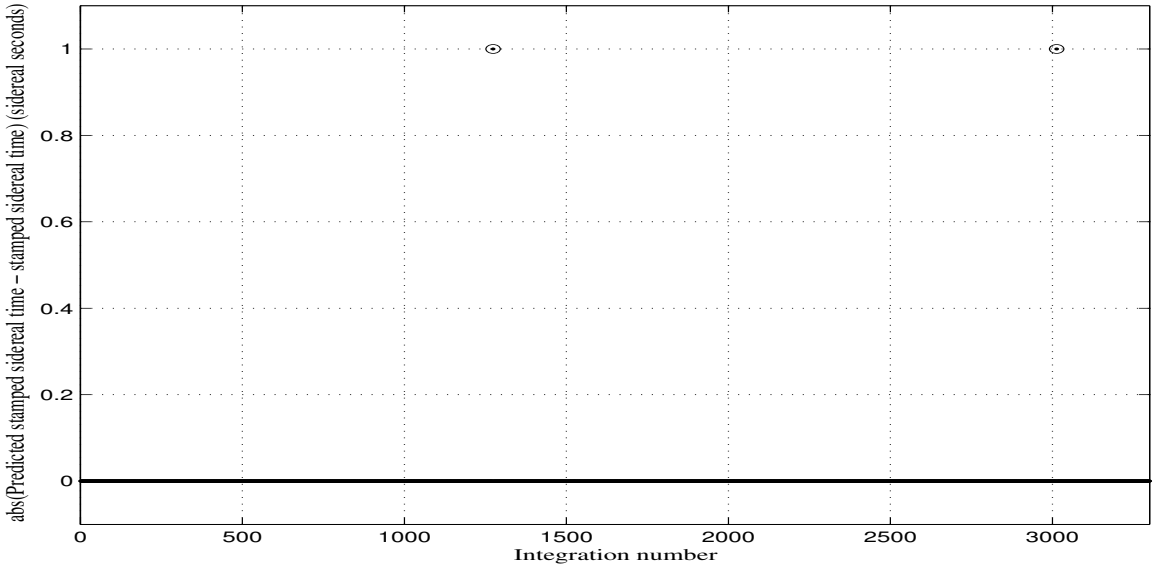

(b) Absolute difference (marked as dots) between predicted sidereal time stamps and the sidereal time stamped in the data file. The difference is zero for all the integration periods except two instances which are shown as $\odot$.

Fig. 5.3: Improvement in the estimation of the sidereal time of the recorded visibilities covering 3307 integration periods (one sidereal hour range duration). The sum of absolute difference between the true sidereal time and the sidereal time stamped for the entire file is 1654 s (mean absolute difference is 0.50 as expected). The sum of absolute difference between predicted sidereal time stamps (using the technique developed) and the sidereal time stamped for the data file is 2 s (mean 0.00064 s). The striking agreement using the developed technique can be seen for all the integration periods except for two cases (shown encircled). In both cases the difference is likely due to the fractional part of the true sidereal time being too close to zero or unity which makes it difficult to correctly estimate the integer part in the developed scheme or due to the precision of the information resolution of the astronomical clock.

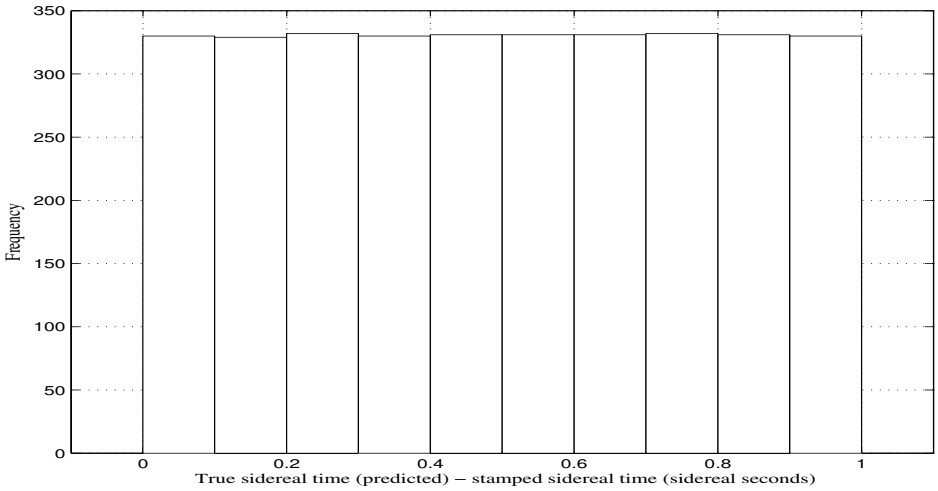

Fig. 5.4: Histogram of difference in the true sidereal time (predicted) and the sidereal time stamped in a data file. It shows that the difference between the true sidereal time and the sidereal time stamped in the data file varies uniformly between 0 to 1 sidereal seconds.

between the true and the observed visibilities. The present calibration technique used at MRT (Dodson, 1997; Golap, 1998; Sachdev, 1999) is based on the observation of well known strong unresolved sources with accurately known positions to calibrate the array. The efficacy of calibration depends upon the calibrator source properties like whether it is resolved or not, its flux density, variability and the accuracy of its known position in the sky. In case the array is unstable, periodic observations are needed to monitor the changes in the gain of the array with time. Although the third cycle of data has been observed in (E+W) $\times$ E and (NS+W)$\times$NS mode to enable calibration using redundant baseline calibration (Hamaker et. al., 1977), this has not been exploited (initial investigations did reveal the usefulness of the scheme though (given in Appendix A of (Golap, 1998))). Since the data from all the three cycles have been used to synthesize the images, presently we have continued to use observation of strong calibrator sources in the sky to calibrate the visibilities.

5.2.1 Fringe calibration

We estimate the visibility phase by fringe fitting, where we assume that the sky in the primary beam is dominated by the calibrator source. The instrumental phase is simply the difference between the phase of the observed visibilities and the expected geometric phase due to a point source (calibrator). The instrumental gain is estimated by measuring the relative amplitudes of the fringes on different baselines. The instrumental phase is insensitive to short term interference and also due to fringes of other sources in the sky provided their fringe rate is significantly different from that of the calibrator for a given

baseline. Therefore at short baselines where there are less than three fringes in the EW group beam (2°) due to the calibrator, satisfactory calibration cannot be obtained (Golap et. al., 1998).

Baselines with short EW component :

For baselines with short EW components, the contribution due to other sources does not average to zero over Hour Angle (HA) range of ±1° (around the calibrator transit) of integration. Also, short baselines are sensitive to the large scale structure of the Galactic background. Therefore, fringe calibration does not work well for baselines with a small EW component, except for very strong calibrators. To estimate the complex gain of these baselines (essentially those formed by the first four East and the West groups) we use closure information obtained with the last EW group E16 (Golap, 1998), assuming there are no amplitude closure errors. Since E16 is multiplied with all the EW groups and all the south groups, the gain of a short baseline like S1E1 is derived from measurements of S1E16 and E1E16 (Golap, 1998; Sachdev, 1999).

$$\frac{G_{S1,E16}G_{E16,E1}}{G_{S1,E1}G_{E16,E16}} = \frac{(G_{S1}G^*_{E16})(G_{E16}G^*_{E1})}{(G_{S1}G^*_{E1})(G_{E16}G^*_{E16})} = 1 \tag{5.2}$$

therefore

$$G_{S1,E1} = \frac{G_{S1,E16}G_{E16,E1}}{G_{E16,E16}} = \frac{|G_{S1}||G_{E16,E1}|e^{j(\phi_{S1}-\phi_{E16})}|G_{E16}||G_{E1}|e^{j(\phi_{E16}-\phi_{E1})}}{|G^2_{E16}|} \tag{5.3}$$

where ϕ refers to the phase, G refers to the complex gain and the subscripts refer to groups forming the baseline. Once the baseline based complex gains are estimated, the antennae based solutions for amplitude and phase are determined. Since the number of baselines are 512 while there are only 48 independent complex antennae gains, this is an over determined system. This improves the estimation of complex gains significantly. The solutions for complex gains of the antennae are obtained using Singular Value Decomposition (SVD).

5.2.2 Calibration sources for MRT

The sensitivity per baseline at MRT is ≈26 Jy (1σ) for a 1 MHz bandwidth and an integration time of one second. In 10 minutes of time which is the time taken by sources at −40° to transit a 2° beam, we get a sensitivity per baseline[3] of about 2 Jy. However, because of contributions from sources other than the main calibrator in the primary beam, we need stronger calibrators to get reliable calibration. Further, the calibrators should have the desired properties that they should be unresolved, non-variable over the time range used for

[3]The non-uniform weighting due to the primary beam has to be taken into account in calculating the sensitivity.

S.No.	Source name (J2000)	Position (J2000) (RA)	(Dec.)	Flux density (Jy) at 408 MHz	160 MHz	150 MHz	Helix beam factor	Attenuated Flux density (Jy) at at MRT
1	MRC0915-118	09 18 05.8	-12 05 44	132.0	243.0	253.4	0.50	126.7
2	MRC1932-464	19 35 57.1	-46 20 44	39.6	91.6	97.0	0.97	94.1
3	MRC2211-172	22 14 25.7	-17 01 44	28.7	79.2	89.9	0.63	56.6

Table 5.1: The calibrators used at the MRT.

calibration, isolated from confusing sources and should have well known measured positions. Table 5.1 has a list of point sources which are confirmed to give reliable calibration. For all practical purposes for the images presented in this dissertation MRC1932-464 has been used for calibration. A few aspects related to calibration using this source are discussed in Sec. 7.3.1.

Apart from the general limitation imposed by the signal to noise ratio of the calibrators and the broad primary beam (leading to substantial contributions from sources other than the main calibrator), there are other factors which affect the calibration of the array like accurate knowledge of band shapes, timing errors, positional errors and stability of the system.

Delay zone calibration :

Due to paucity of strong sources we have not been able to independently calibrate the visibilities measured with different delay settings. Using the receiver configuration a procedure was developed by Sachdev & Udaya Shankar (2001b) for estimating the instrumental phase in the four delay zones using a calibrator in only one of the delay zones. This needs information about the centroids of the bandpasses of each baseline. They measured the bandpasses and estimated the variation in the centroids of the bandpasses of the 512 baselines used for imaging. They established that variation causes only a 5°rms error in the instrumental phase calibration.

Salient features of calibration at MRT :

The primary beam modulates the fringe pattern of the calibrator source. Thus the fringes closer to transit have more signal than the ones away from the transit. There are two factors competing in deciding the signal to noise ratio in the fringe calibration. They are the increased stretch of time available for a lower declination source and the primary beam attenuation factor which attenuates sources at declinations away from -40°. Thus while calibrating, a data length appropriate to the calibrator declination is chosen. The ability to filter away the effect of other point sources in the fringes depend both on the declination of the calibrator and the declination differences with the interfering point sources. As the fringe frequency is $\cos(\delta)$ dependent, the rate of change of fringe frequency, with change in declination, is slowest at $\delta = 0^o$ and fastest at $\delta = -90^o$. Thus for baseline consisting of the extreme East group (E16) and a NS group (S1 say), sources 20^o away will be filtered

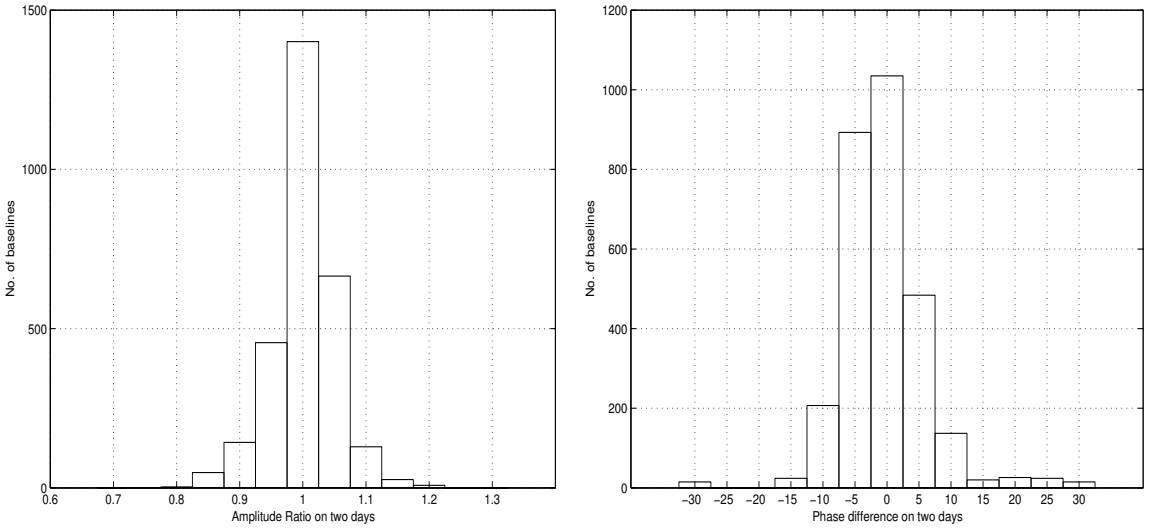

(a) Amplitude ratio

(b) Phase difference (degree)

Fig. 5.5: Histogram of the ratio of amplitude (a) and difference in phase (b) of the instrumental gains of the baselines, estimated using MRC0915-118 on two consecutive days (based on six pairs of data files). The day to day rms variation per baseline in amplitude is ≈5% and phase is ≈8°.

if calibrator is on the equator. However, if the calibrator was near the pole then effects of sources only 4^o away would be filtered effectively[4]. Correlator offsets do not affect the ability of fringe calibration, especially if there are more than three fringes.

5.2.3 The amplitude and phase stability of the array

As mentioned earlier due to paucity of suitable calibrators, we can calibrate our array only three times a day using the calibrators given in Table 5.1. In addition, the solar activity, man made interference, occasional interruptions in observations due to instrumental malfunctioning, power failures etc., often limits the possibility of applying the calibration process to less than three times a day. Hence, we apply the estimated complex gain using observations of the calibrators to calibrate the observed visibilities at some other sidereal time during any continuous stretch of observation. To enable us to do so the system stability is very critical i.e. the complex gain of the array must not vary with time beyond acceptable limits. In this context we now discuss the amplitude and phase stability of the array.

To estimate the amplitude and phase stability of the array we compare the amplitude and phase per baseline obtained by the same calibrator source on two consecutive days when the observations have been continuous without any interruption. Histograms of the day to day variation of amplitude and phase per baseline estimated using the calibrator

[4]Also termed as declination filtering by Golap (1998).

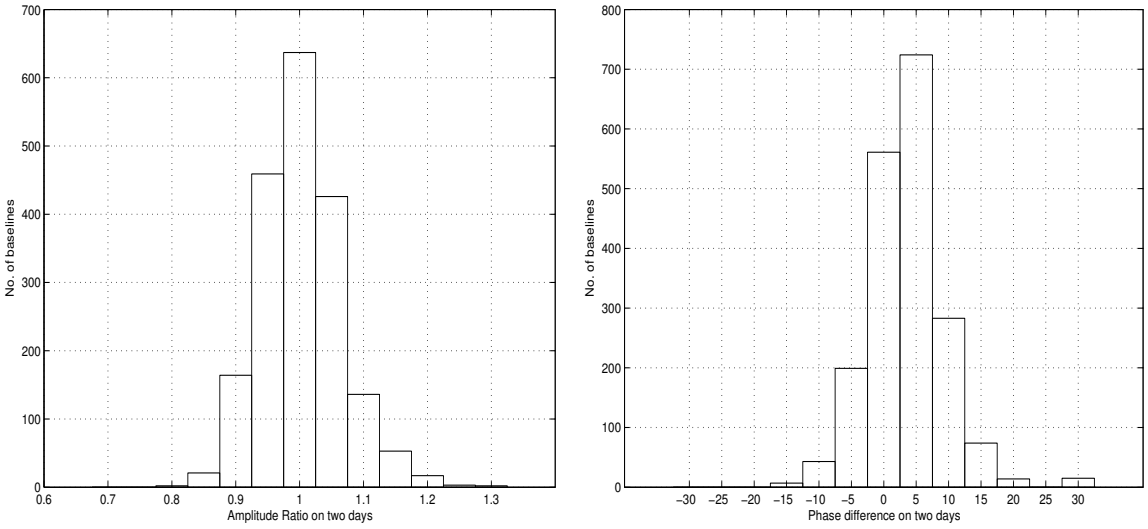

(a) Amplitude ratio (b) Phase difference (degree)

Fig. 5.6: Histogram of the ratio of amplitude (a) and difference in phase (b) of the instrumental gains of the baselines estimated using MRC1932-464 on two consecutive days (based on four pairs of data files). The day to day rms variation per baseline in amplitude is ≈6% and phase is ≈6°.

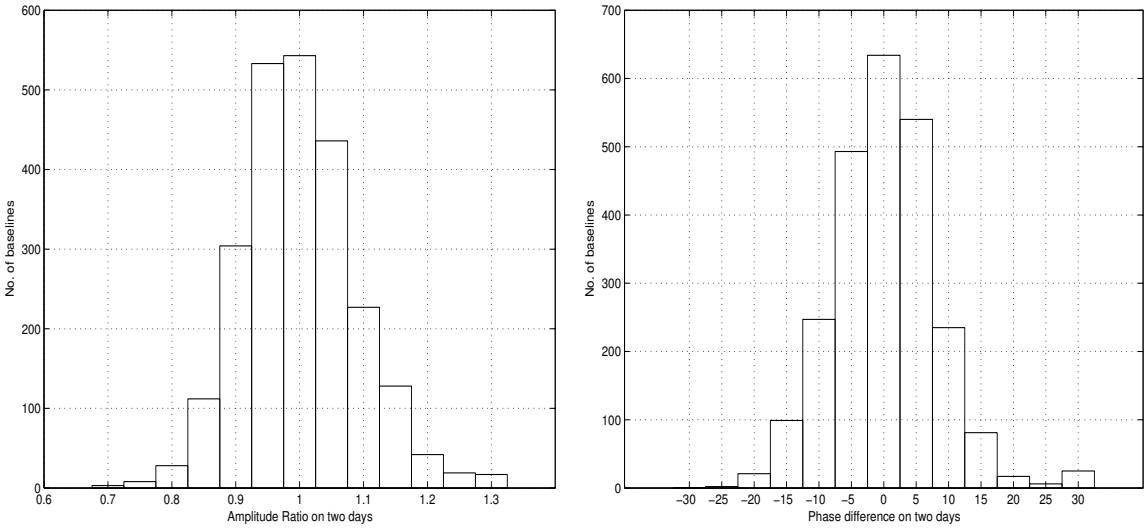

(a) Amplitude ratio (b) Phase difference (degree)

Fig. 5.7: Histogram of the ratio of amplitude (a) and difference in phase (b) of the instrumental gains of the baselines estimated using MRC2211-172 on two consecutive days (based on five pairs of data files). The day to day rms variation per baseline in amplitude is ≈9% and phase is ≈8°.

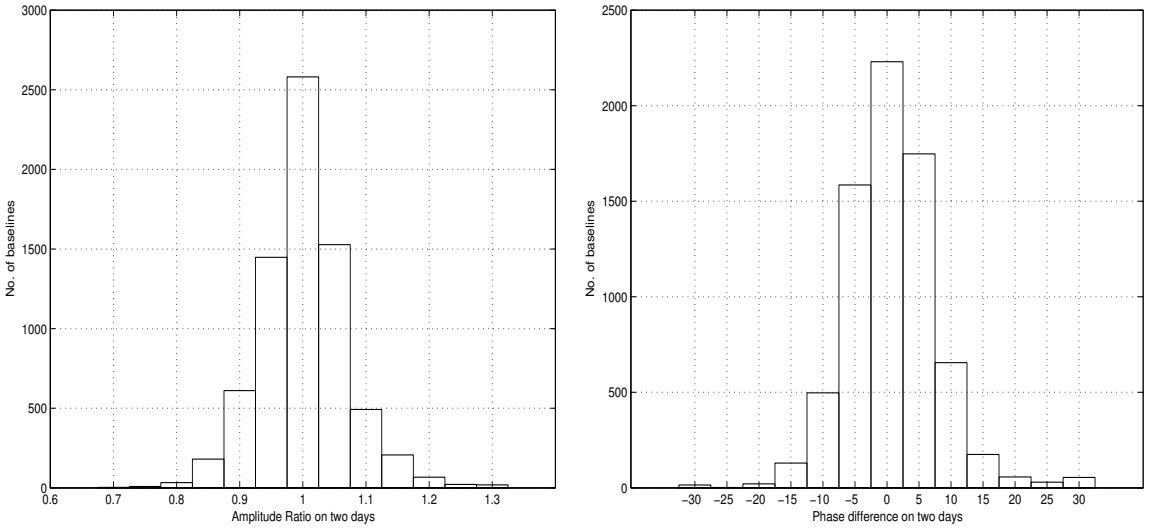

(a) Amplitude ratio

(b) Phase difference (degree)

Fig. 5.8: Histogram of the ratio of amplitude (a) and difference in phase (b) of the instrumental gains of the baselines estimated using the same calibrator for all the three calibrators mentioned in Table 5.1(based on sixteen pairs of data files). The day to day rms variation per baseline in amplitude is ≈7% and phase is ≈8°.

sources MRC0915-118, MRC1932-464 and MRC2211-172 on two consecutive days is shown in Fig. 5.5, Fig. 5.6 and Fig. 5.7 respectively.

The day to day rms variation per baseline estimated using calibrator MRC0915-118 in amplitude is ≈5% and phase is ≈8° as shown in Fig. 5.5 (based on six pairs of data files on two consecutuve days). For MRC 1932-464 the day to day rms variation per baseline in amplitude is ≈6% and phase is ≈6° as shown in Fig. 5.6 (based on four pairs of data files on two consecutuve days). The day to day rms variation per baseline estimated using calibrator MRC2211-172 in amplitude is ≈9% and phase is ≈8° as shown in Fig. 5.7 (based on five pairs of data files on two consecutuve days). Fig. 5.8 shows the day to day amplitude and phase variation of the array when the amplitude ratio and phase difference estimated using all the three calibrators are considered together. The day to day variation per baseline in amplitude is ≈7% and phase is ≈8°. From the comparison we see that the typical phase variation per baseline from one day to the next day for the same calibrator is in the range of ≈5-10°, while the amplitude variation is in the range of ≈ 5-10%.

Next, we compared the instrumental phases estimated using two different calibrators (at different declinations) on the same day for phase errors which are baseline based (including due to relative positions of NS groups and the EW groups) and declination dependent errors etc.. Histograms of the phase differences estimated using

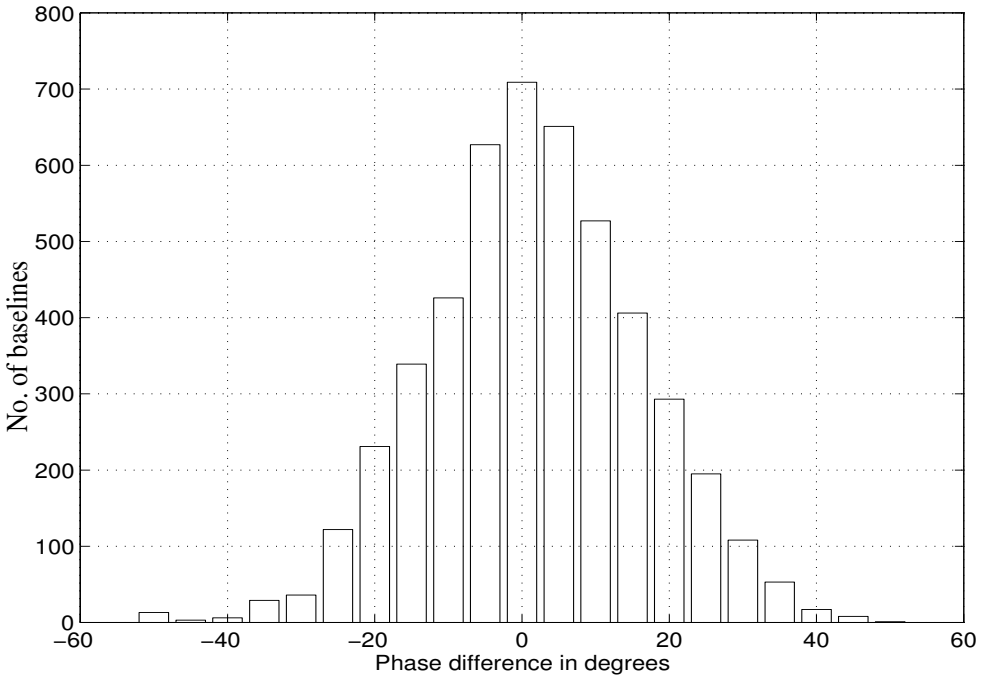

Fig. 5.9: Histogram of the difference in instrumental phases estimated using two different calibrators MRC2211-172 and MRC0915-118 on the same day (based on ten pairs of data files). The rms variation in phase per baseline is ≈12°.

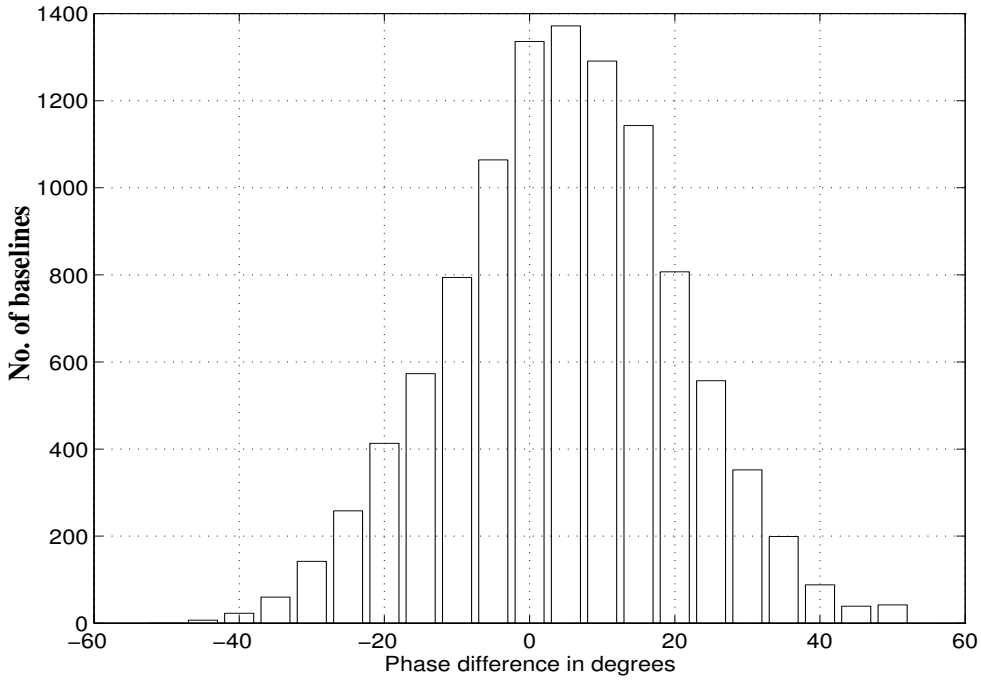

Fig. 5.10: Histogram of the difference in instrumental phases estimated using two different calibrators MRC1932-464 and MRC2211-172 on the same day (based on twenty two pairs of data files). The rms variation in phase per baseline is ≈14°.

two different calibrators is shown in Fig. 5.9 (using MRC2211-172 and MRC0915-118) and Fig. 5.10 (using MRC1932-464 and MRC2211-172). The difference in instrumental phases estimated using MRC2211-172 and MRC0915-118 has an rms variation per baseline in phase of ≈12° (based on ten pairs of data files). The difference in instrumental phases estimated using MRC1932-464 and MRC2211-172, has an rms variation per baseline of ≈14° (based on twenty two pairs of data files). These amplitude and phase variations mentioned here also include the effect of ionospheric variations over time and the errors due to delay zone calibration as discussed earlier.

In a nutshell the day to day rms variation of amplitude and phase per baseline estimated using the same calibrators is within the range 5% to 10% and 5° to 10° respectively. The rms phase variation per baseline when estimated using different calibrators on the same day is in the range of 10° to 15°. Each day's image is synthesized using 480 (32EW×15NS) visibilities. The expected dynamic range limitation due to a phase variation of 15° is $15\times\frac{\pi}{180}\times\frac{1}{\sqrt{32\times15}}\approx\frac{1}{84}$. The final image would be synthesized by 63 allocations (≈32×880 baselines). The expected dynamic range limitation for the final image is $\approx\frac{1}{640}$. This is quite acceptable and in fact we would be dynamic range limited by other factors like rms noise and accuracy in the estimation of the PSF.

5.3 Wide field imaging with MRT

Once the visibilities are calibrated by the method of *fringe calibration* as described earlier the next step is to transform them to obtain the dirty images. The relationship between the calibrated visibility ($V(u,v,w)$) and the sky brightness ($I(l,m)$) is given by the relation,

$$V(u,v,w)=\int\int I(l,m)A(l,m)\,e^{-j\,2\pi(ul+vm+w\sqrt{1-l^2-m^2})}\frac{dl\,dm}{\sqrt{1-l^2-m^2}} \tag{5.4}$$

where u,v,w are the projected coordinates of the antennas, l,m,n are the direction cosines in the uvw co-ordinates system and $A(l,m)$ is the product of the voltage patterns of the antenna elements forming the baselines. Eqn. 5.4 is not a Fourier transform relation and it is not straightforward to invert this equation. $V(u,v,w)$ is a 3-D function while $I(l,m)$ is only a 2-D function. For small fields of view ($l^2+m^2\ll1$) the visibility function is related to the sky brightness by a 2-D Fourier transform. However, when this condition is not satisfied and if we still consider the usual 2-D Fourier transform, the third variable manifests itself when the w term becomes significant. Thus the image plane can no longer be expressed as a 2-D Fourier transform of the visibility function and must be modeled as a surface of a sphere referred to as the celestial sphere by treating $\sqrt{1-l^2-m^2}$ as an independent coordinate.

A full 3-D treatment of the problem is required to make images (Perley, 1999). A full 3-D Fourier transform of $V(u,v,w)$ gives us what is referred as the three dimensional 'image volume'. The brightness distribution $I(l,m)$ can be shown to be related to the image volume $F(l,m,n)$ as,

$$F(l,m,n) = \frac{I(l,m)\,\delta(\sqrt{1-l^2-m^2}-n)}{\sqrt{1-l^2-m^2}} \tag{5.5}$$

where δ is the Dirac delta function. The 2-D sky brightness distribution can be recovered from this image volume and this method is popularly known as 3-D inversion. The sky brightness distribution is a function of two variables and the third variable n is introduced solely to establish a formal Fourier relation. The image volume $F(l,m,n)$ is a function of three variables, but the only physically meaningful quantities within it lie on the sphere of unit radius defined by $n = \sqrt{1-l^2-m^2}$. Since in practice, the visibilities are sampled at some discrete locations of the visibility function over a finite range and could be measured with different weights, we introduce a weighting function $S(u,v,w)$ also known as the spectral sensitivity function or the transfer function with which the visibilities are multiplied. Therefore the image volume $F(l,m,n)$ gets convolved with $P(l,m,n)$ which is the Fourier transform of $S(u,v,w)$.

$$F(l,m,n) = \frac{A(l,m)\,I(l,m)\,\delta(\sqrt{1-l^2-m^2}-n)}{\sqrt{1-l^2-m^2}} \star\star\star P(l,m,n) \tag{5.6}$$

where $\star\star\star$ represents a three dimensional convolution. On the sphere where $n = \sqrt{1-l^2-m^2}$, the dirty image of the brightness distribution $I_d(l,m)$ is,

$$I_d(l,m) = \frac{A(l,m)\,I(l,m)}{\sqrt{1-l^2-m^2}} \star\star P(l,m) = \int\int\int S(u,v,w)\,V(u,v,w)e^{j2\pi\left(ul+vm+w\left(\sqrt{1-l^2-m^2}\right)\right)}\mathrm{d}u\mathrm{d}v\mathrm{d}w \tag{5.7}$$

where $P(l,m)$ is the synthesized beam and is a direct consequence of the visibilities being measured over a limited range of u,v,w, i.e., with some spectral sensitivity function $S(u,v,w)$. In transforming the visibilities to brightness, it is convenient to use the Fast Fourier Transform (FFT) algorithm. This, however, requires the visibilities to be measured at regular intervals. In many arrays, the visibilities are not measured at regular intervals on the $(u,\ v)$ plane. Hence, one cannot directly use the FFT. In such a case, one can perform the transform using a Direct Fourier Transform (DFT) which however takes a longer time being computationally expensive. Alternatively, one can 'grid' the measured visibilities onto a uniformly sampled plane and then apply the FFT. Gridding involves interpolation of the available points and giving some value where no data points exist within a grid unit.

Now we discuss the inversion of visibilities for obtaining the brightness distribution at MRT to obtain the wide field images.

5.3.1 Meridian transit imaging

The sampling of the visibilities in the EW direction is at intervals equal to the size of the each EW group (64 m). This gives grating responses (at equal intervals of $\Delta l = \frac{\lambda}{64}$) which fall on the nulls of the primary beam of the EW group while synthesizing on the meridian. But when the image is synthesized away from the meridian one of the grating response starts moving into the main lobe of the primary beam of the EW group. This leads to the synthesizing beam, being a function of the hour angle. To simplify matters, imaging is presently done on the meridian only. The scanning in RA is provided by the motion of the earth. The raw image on the meridian ($l = 0$) along the declination is given by,

$$I_d(m) = \int\int\int S(u,v,w)V(u,v,w)e^{j2\pi\left\{vm+w\left(\sqrt{1-m^2}\right)\right\}}\mathrm{d}u\ \mathrm{d}v\ \mathrm{d}w \tag{5.8}$$

At MRT the visibility coverage at each instant can be thought of as a pleated sheet, extended both in u and v with discrete steps in w, as we move from one EW group to another EW group at a different height. The 2-D image is the combination of 1-D stacks along the meridian at different sidereal times. The equation for inversion of visibilities involves DFT and is computationally expensive. There have been various techniques proposed for recovering the sky brightness distribution from the visibility data obtained with a non-coplanar array with lesser computation. One such technique is Tangent Plane Approximation (TPA). We briefly discuss its applicability for inversion of visibilities for MRT in the following section.

5.3.2 Limitation of TPA for inversion of visibilities

We know that for small fields of view the relationship between the visibility and brightness distribution can be approximated by a two dimensional transform. In the approach of Tangent Plane Approximation we repeatedly apply this small field approximation, so that the celestial sphere is approximated by a number of tangent planes (Perley, 1999).

In order to get an actual estimate of the errors if the TPA is used to synthesize the dirty image, a simulation study was carried out by Oozeer & Udaya Shankar (2002). We summarize the main inferences from their studies.

Phase errors leading to amplitude errors : They considered tangents at various zenith angles (za) and corrected for phases at different points on the tangent for heights as seen by the source at the tangent point. The response of the sources on the tangent away from the

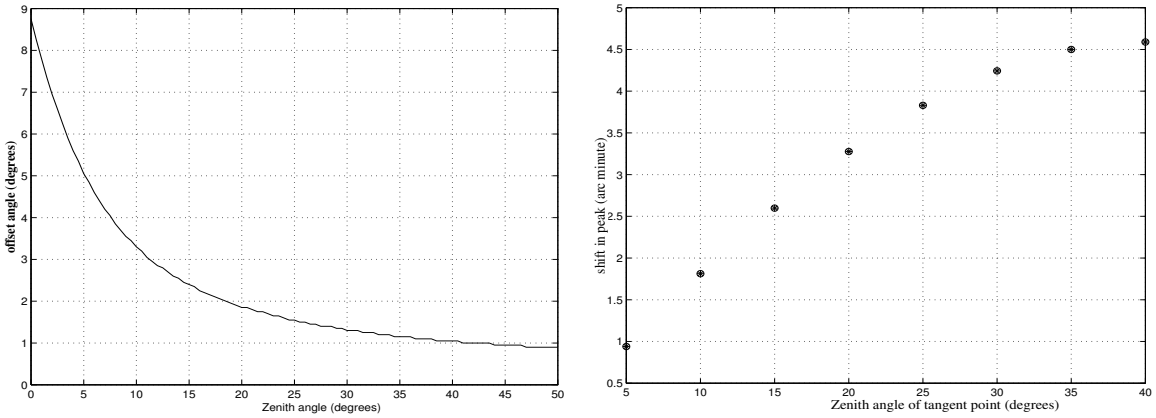

(a) This plot shows the zenith distance from the tangent point for various zenith angles at which the strength of a source falls to 90% of its true value due to the TPA.

(b) This plot shows the shift of the source away from the meridian for an offset angle of 5° as a function of the zenith angle of the tangent point.

Fig. 5.11: Loss of amplitude and shift in position due to phase errors with TPA (Oozeer & Udaya Shankar, 2002).

tangent point was examined. Fig. 5.11(a) shows the zenith distance from the tangent point at which the attenuation in amplitude is 10% for tangents at various zenith angles. We note that for the tangent plane at $za = 50°$, the amplitude of a source on the tangent only at a zenith distance of 1° from the tangent point is attenuated by 10%. Their simulations also revealed that for a zenith distance of 5° for the tangent plane at $za = 50°$, the attenuation increases to ≈35% which is quite significant and unacceptable.

Phase errors leading to position errors : The 2-D PSF of a source transiting the meridian was examined for various zenith distances on the tangent, from the tangent points at different zenith angles. The peak of the PSF of a source at the tangent point was as expected on the meridian. For sources on the tangent but away from the tangent point the peak of the 2-D PSF was shifted away from the meridian. This happens due to geometry of the MRT array (see Oozeer & Udaya Shankar (2002) for details). Fig. 5.11(b) shows the shift in the peak of PSF of a source on the tangent at a zenith (offset angle) distance of 5° from the tangent points considered at various zenith angles. We note that for a tangent at za=40°, for a source on the tangent which is at a zenith distance of 5°, the shift in the peak (i.e. the positional error) is ≈4′.6. This is quite comparable to the resolution of the MRT array and unacceptable.

The loss in amplitude and position errors of the sources due to the phase errors clearly reveal that the TPA is not desirable for inversion of visibilities to brightness distribution even if we use six tangent planes, each of ±5° in order to cover the entire declination range

of MRT.

Imaging using Direct Fourier Transform :

The large number of facets or tangent planes required in order to image the wide field would make the imaging and deconvolution complicated and cumbersome. Due to this TPA was not considered appropriate and the brute force approach using Fourier phasing (via DFT) is implemented for imaging. The calibrated visibilities are rephased at each point along the declination on the sky at transit, (*i.e.* on the meridian) and combined to get the dirty image at that point. This is represented by the following equation.

$$I_t(m) = \sum_u \sum_v \sum_w V(u,v,w) \times e^{j2\pi\left(v.m+w.\sqrt{1-m^2}\right)} \tag{5.9}$$

where $I_t(m)$ is the dirty image on the meridian at sidereal time t. The heights and distances measured along the track are used. This method is expensive in terms of computation but there is no assumption either of the regular sampling of the visibilities nor about any slope of the track. So all the parts of the tracks are treated in a uniform way. The observed visibility data has Hermitian symmetry since the image is real. So, only the real part of the above image is considered as the dirty image of the brightness distribution of the sky. The imaginary part is also generated and is used to cross check the calibration by making sure that imaginary part is zero at the transit time of the calibrator. The images presented here have been synthesized by this method of direct phasing.

Look-up tables for DFT :

In order to decrease the computation time for DFT, we optimized the imaging process via use of look-up tables for the trigonometric functions (See Sec. 2.3.2). The major time spent in DFT is in computation of the trigonometric functions *sine* and *cosine*. Since we carry out meridian transit imaging in a priori known fixed directions on the meridian, the trigonometric functions needed for the inversion at any instant is for the same angles for all sidereal times. At the start of the inversion of visibilities all the required trigonometric functions were directly computed and stored in an static associative array whose life time was same as life of the program since invocation. During the inversion of the visibilities at subsequent sidereal times the required values of the trigonometric functions were straight away fetched from the associative array. Since retrieving the value from virtual memory is much faster than undergoing an expensive computation of a trigonometric function, this resulted in bringing down the time required for inversion of visibilities for an allocation covering one sidereal hour range on a 2.4 GHz PC by a factor of ten, from ≈50 min to ≈5 min.

5.3.3 Imaging guard zones along RA

As mentioned earlier the dirty images are synthesized on a sidereal hour basis for each allocation. Since the observations have been carried out over a long period of time (nearly five years), the images for different allocations for a given sidereal hour range are in different epochs. Due to this, the actual region of overlap (in any common epoch) for which the full resolution image can be obtained by adding all the individual allocation images is less than one full sidereal hour range (due to different amount of precession for each allocation's image). In addition, we need images of adjoining regions on both the sides in RA as guard zones to successfully deconvolve the dirty image near the boundaries of the sidereal hour range under consideration. In view of this for each allocation's image the visibilities on both the sides of the sidereal hour range under consideration are also imaged separately by the same data processing steps. Later the three one day images for each allocation corresponding to the preceding sidereal hour range, central sidereal hour range and following sidereal hour range (made with data from continuous observation stretch on the same day) are joined along RA to obtain the allocation's image covering nearly three sidereal hours in RA. All the days on which the images for a given allocation for adjacent sidereal hours are not available on both the sides as per the desired criteria, are not considered for further analysis. *From now onwards any allocation's image or a day's image would refer to an image corresponding to one sidereal hour range along with additional guard zones (covering $\approx$54 min) on both sides in RA. These guard zones also help in scaling the images of different sidereal hours to a common level (See Sec. 7.2.1.1).*

5.4 Combining different sets of observations

Each day's image is subjected to sieve remaining RFI as discussed in Chapter 4 (See Sec. 4.3.5). Before combining images on different days to obtain full resolution dirty image with appropriate weights, we need to take into account the following aspects. Images made on different days are in different epochs as the observations for the survey have been carried out over a period of five years. It is also essential to analyse each day's image to estimate the relative weights for addition and to identify and reject images which are corrupted. In addition, the images corresponding to different allocations suffer different bandwidth decorrelation at different position in declination and need to be combined with appropriate delay zones to minimize the net bandwidth decorrelation in the full resolution image. These aspects are discussed in the next few sections.

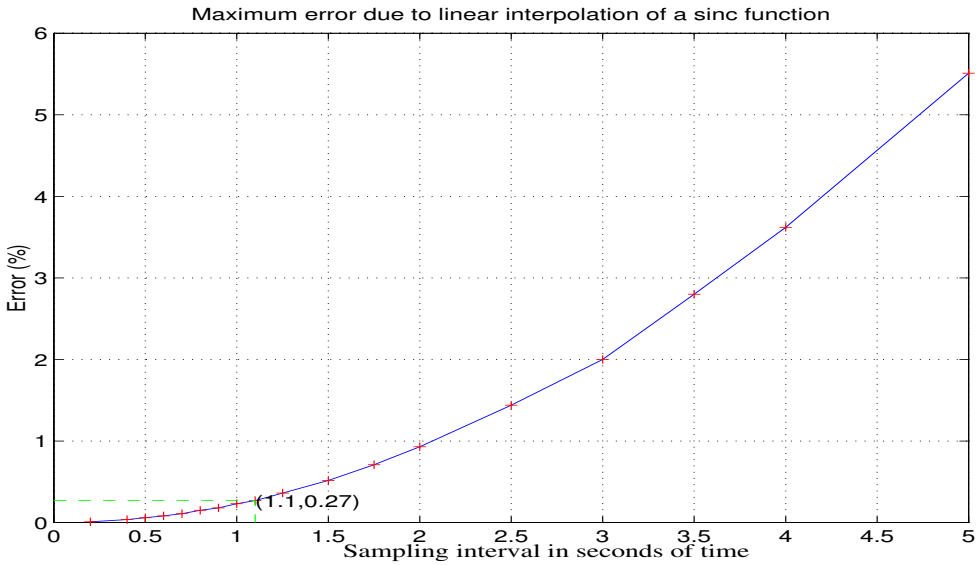

Fig. 5.12: The plot shows maximum error due to linear interpolation of a *sinc* function of FWHM 16 s as a function of sampling interval. The maximum error corresponding to the sampling in our case (every 1.1 s) is only 0.27%.

5.4.1 Box-car averaging, precession and regridding

Each day's image is box-car averaged for 4 s. Interference detected at all stages during data processing (up to the level of each day's image before post-integration) is incorporated at this stage, in each day's image by giving zero weights to the points affected by interference. All one day images after box-car averaging are precessed and regridded to a uniform common grid in the epoch J2000. The common grid has 900 points in RA in one sidereal hour range and 4096 points along $\sin(za)$ which extends from -1 to +1. This translates to ≈2300 points for declination range -70° to -10° of interest to MRT.

The precession is different for different images depending upon the day of observation. Precession is a nonlinear function of RA and declination. The precession of dirty images causes the sidelobes of a source to be precessed differently than the main beam. The effect of precession on Point Spread Function (PSF) has to be taken into account during deconvolution. This is discussed in Sec. 6.3.2.3.

The process of box-car averaging and regridding using linear interpolation introduces errors. The maximum error introduced due to box-car averaging a *sinc* function (FWHM 16 s) for 4 s can be up to ≈0.6%. The maximum error due to linear interpolation of a *sinc* function (FWHM 16 s), as a function of sampling interval is shown in Fig. 5.12. The maximum error corresponding to our sampling (every 1.1 s) is ≈0.27%. Since the inaccuracies introduced due to linear interpolation are much lower compared to errors due to box-car

averaging, higher order interpolation was not considered. In addition we wanted to ensure that in case there is occasional interference remaining in the image, it does not spread due to higher order interpolation to the adjacent sidereal times. The combined effect of errors due to box-car averaging and linear interpolation in the images is within 0.7%.

Once the individual post-integrated images of different days are precessed to the epoch J2000 on a common grid, all the images in a batch are collectively subjected to RFI mitigation as described in Sec. 4.3.6. A batch comprises of images for a given sidereal hour range corresponding to all the allocations for one declination (delay) zone. Before combining images we analyse them in order to ensure that individual images which are corrupted are not included for obtaining the full resolution dirty image.

5.4.2 Analysis of each allocation's image

Image analysis is a general term and the choice of techniques for image analysis depends upon the nature of observations and the objectives for which the interpretation is carried out. In our case each image is subjected to various checks to ensure that images with spurious features, relatively high rms noise etc., are not included during the co-addition.

Displaying data in a variety of ways helps to appreciate it better. We use visualization in conjunction with other techniques for image analysis. A flow chart depicting the analysis in batch mode is shown in Fig. 5.13 where a batch includes images of all the allocations corresponding to one sidereal hour range and one delay zone. Thus for each sidereal hour range there are four batches of images each corresponding to one delay zone. Fig. 5.14 shows some of the various checks each day's image[5] is subjected through and are discussed below.

Model Fitting using unresolved sources :

The sensitivity of each day's image is ≈1.25 Jy. Taking into consideration the primary beam response of the helix, the bandwidth decorrelation and assuming a spectral index of 0.7 for all the MRC sources, the number of MRC sources which are detectable with a signal to noise ratio of 5 in each day's image for different sidereal hour ranges and the entire declination range of MRT are shown in the Fig. 5.15. It shows that there are sufficient number of sources in all the sidereal hour ranges to check and calibrate each day's image. Since the number of sources shown is for the entire declination range of MRT, for an image synthesized for one delay zone, the actual number of sources expected to be seen are actually lesser on an average by a factor of four.

As a first step in the analysis, a list of point sources which are expected to be detected

[5]We recall that it refers to an allocation's images covering one sidereal hour range along with additional guard zones on both sides in RA.

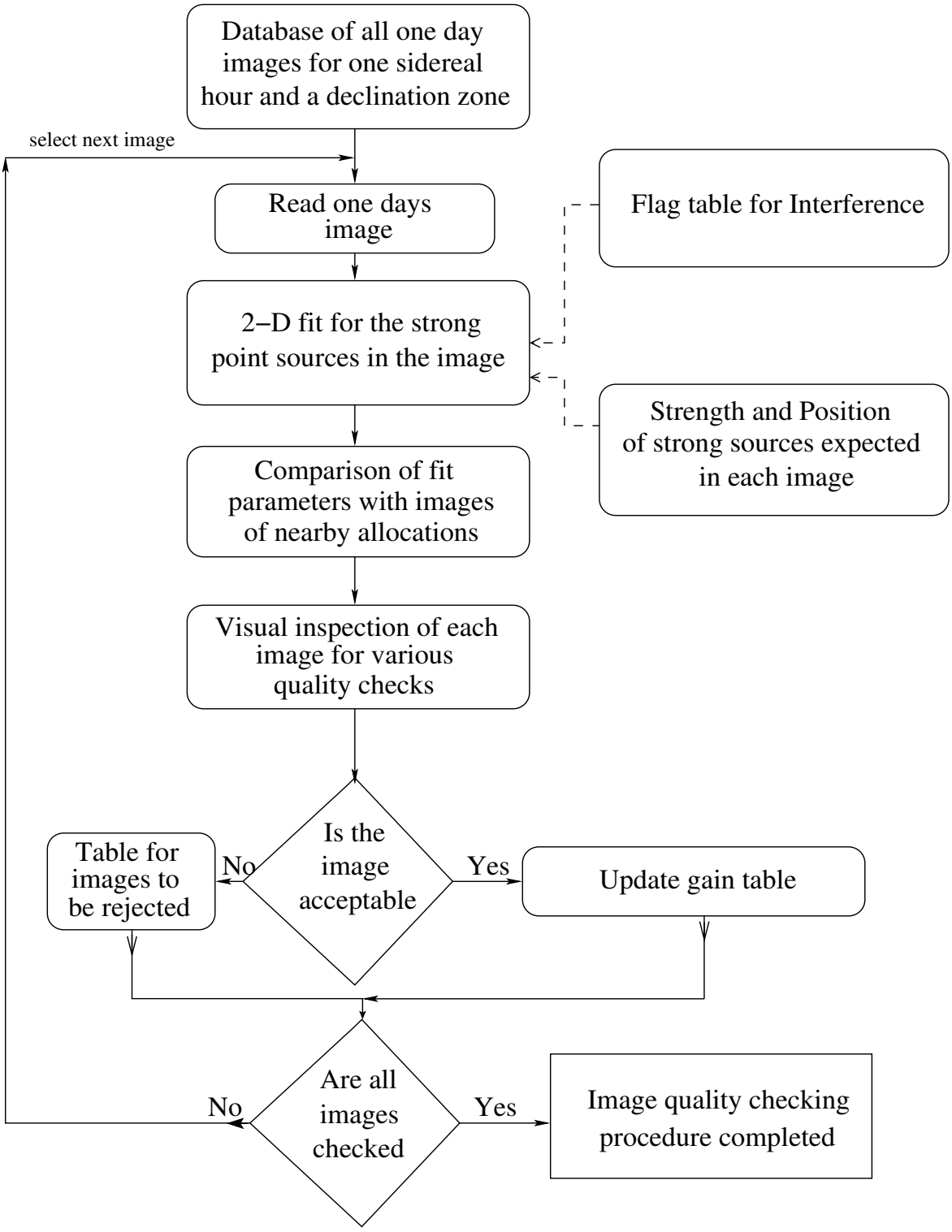

Fig. 5.13: Flow chart showing the steps involved to analyse and check the quality of each allocation's image in a batch.

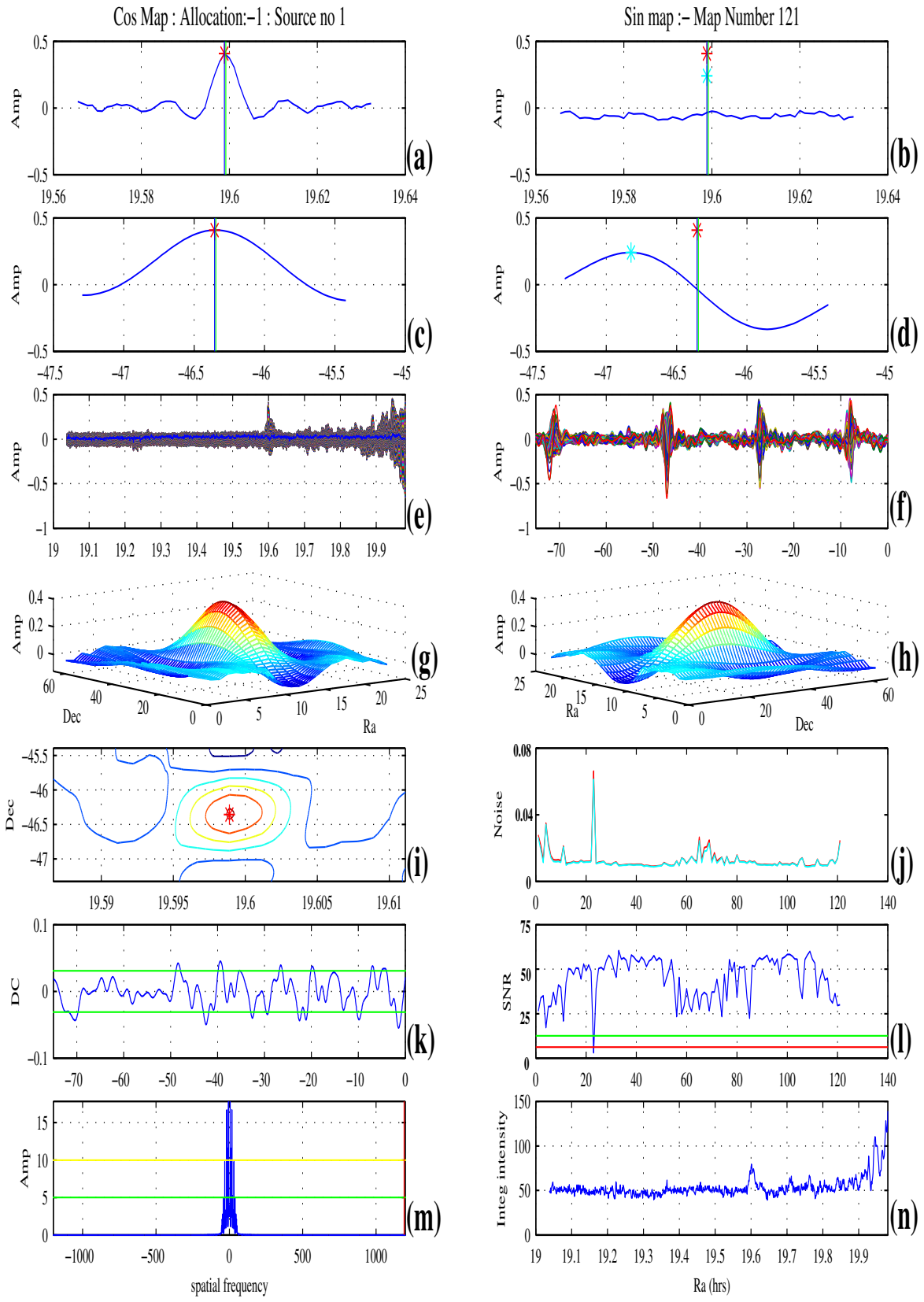

Fig. 5.14: Various quality checks performed before accepting an image for further processing.

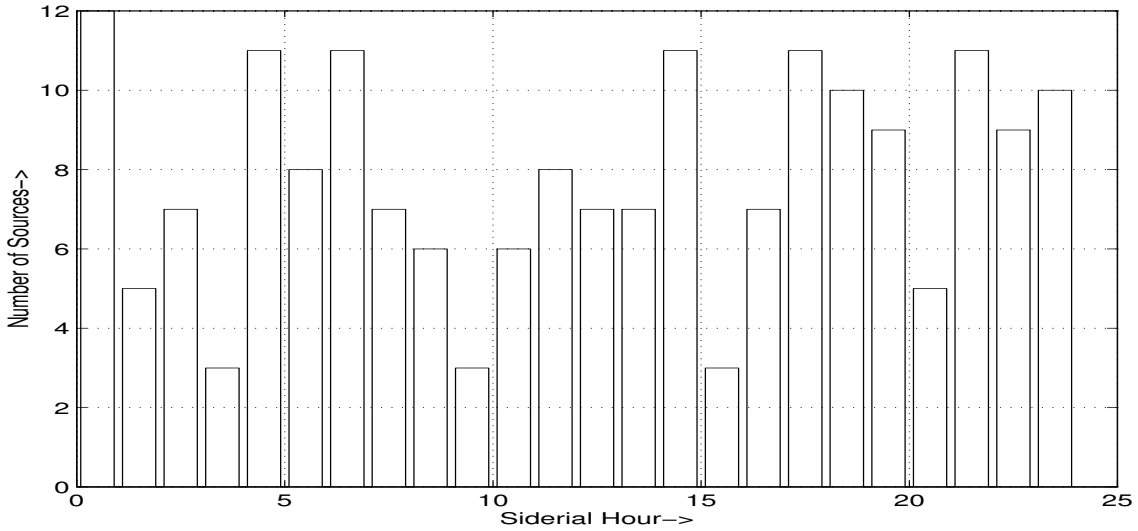

Fig. 5.15: The plot shows number of MRC sources in different sidereal hours, which can be detected with a minimum signal to noise ratio of 5 in each allocation's image.

in a given sidereal hour with peak intensity $\geq 5\sigma$ is made using the MRC catalogue corresponding to the sidereal hour range and declination range of interest. Each image is checked for the presence of these well known unresolved sources and a two dimensional fitting is carried out using the expected beam of the array (PSF). The free parameters during the fit are the peak flux density of the source and its position in RA and declination. The DC offset, is estimated from the background and kept constant during the fitting. Fig. 5.16 shows the measured and the fitted curve for the source MRC1932-464. The lower plot shows the one dimensional cut along RA of the fitted and measured intensity around the measured peak.

It is difficult to explicitly display the 2-D surface of the measured and fitted intensity superposed on the same graph. Due to this the 2-D measured and fitted intensity is represented on a 1-D plot to make the fit more explicit. From the detected peak on both the sides in the image a region in the image equivalent to FWHM of the synthesized beam is considered along RA and declination. The 1-D scans along RA at each declination pixel (in the scan along declination at the detected peak) starting from the first pixel to the last pixel in the region considered are plotted (blue) side by side one after another (next to each other). The corresponding value of the 2-D fitted beam is also shown (red). This way of displaying a 2-D fit gives a very explicit view to visually ascertain the quality of fit. Any image in which these bright well known sources are not present, within the expected positional bounds (HPBW of the synthesized beam) or the obtained signal to noise ratio (Fig. 5.14(l)) is relatively low (poor, less than 2.5 times compared to the images of nearby allocations) is rejected.

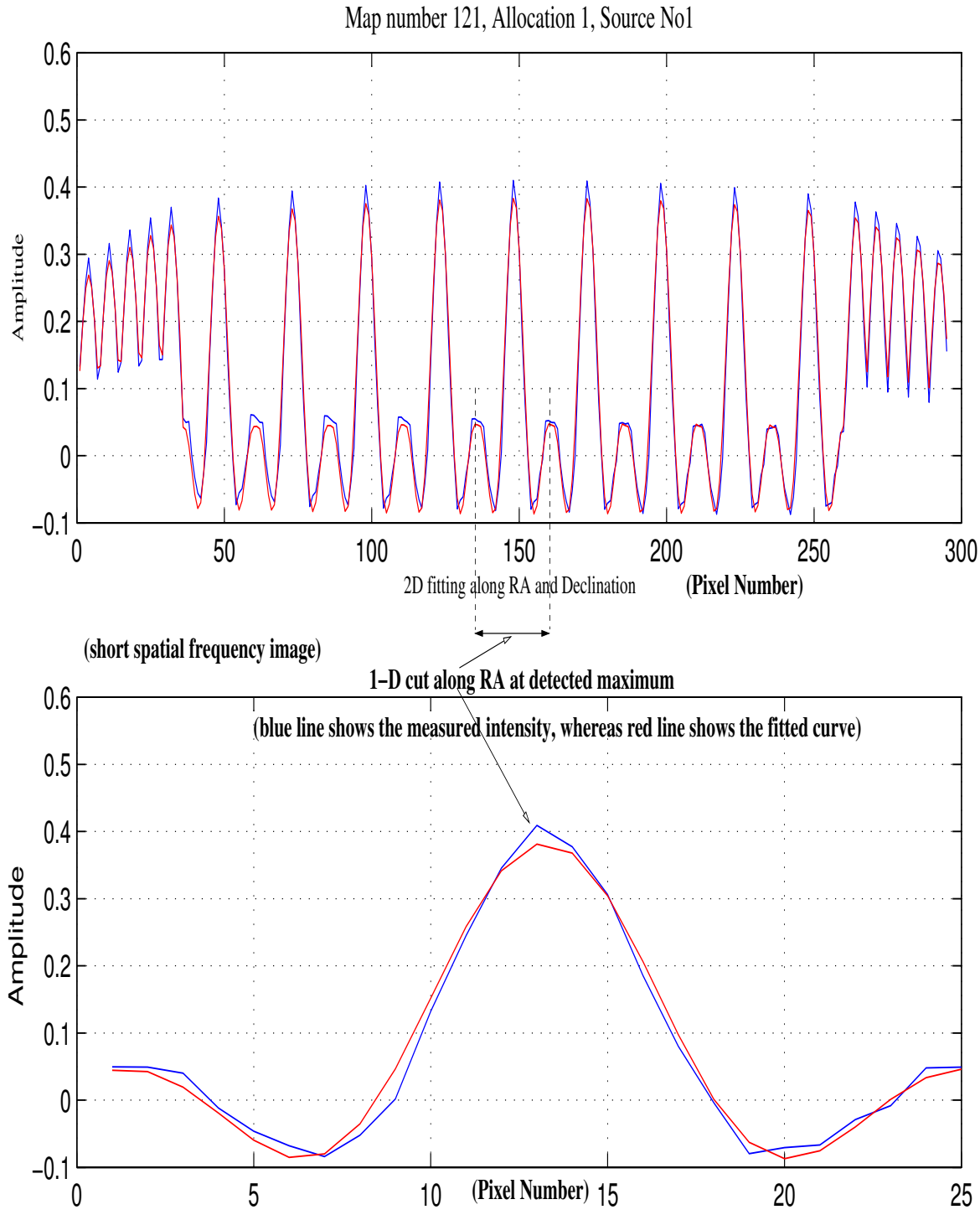

Fig. 5.16: The figure shows the fitting for a strong source in one allocation's image. The top plot shows the 2-dimensional fit while the bottom plot shows the one dimensional cut of the fit at the source peak along RA. The blue is the measured intensity in the image while the red is the fit obtained using the expected beam. The amplitude on the y axis is in arbitrary units. In the x-axis pixel numbers are shown. The 2-D fit is represented (in the top plot) in 1-D (to make the fitting explicit) by placing the adjacent scans (at different declinations) along RA symmetrically on either sides of the detected source peak.

Inspection of real and imaginary cuts :

The Fig. 5.14(a) and Fig. 5.14(c) show one dimensional cuts of the real (cos) part of the complex image as a function of RA and declination respectively at the detected peak of the strong source. The corresponding one dimensional cuts of the imaginary part of the image are shown in Fig. 5.14(b) and Fig. 5.14(d). At the detected peak of the source while a maximum is expected in the real image, the intensity in the imaginary part at the corresponding location is expected to be near zero. The real and the imaginary parts of the image are used to cross check the calibration. Images which show significant departure (more than FWHM) from this expected behavior are most likely a result of improper calibration and are rejected.

2-D profile and contour image :

A two dimensional image (profile plot) of the strong source as a function of RA and declination are shown in Fig. 5.14(g) and Fig. 5.14(h) as seen from different viewing angles. The contour image of the same region is also shown in Fig. 5.14(i). These are essential in determining the general features in the intensity distribution around the point source which are amenable to analysis and help to visually examine spurious features if any.

1-D scans along RA and declination :

One dimensional cuts along RA at all declinations and along declination at all RAs superposed are shown in Fig. 5.14(e) and Fig. 5.14(f) respectively. This helps to identify any unexpected patterns such as sudden DC level shifts and may help in identifying peaks due to interference at unexpected RA and declination.

Aliased images :

The images (for one allocation) under discussion have their visibilities measured with a 6 m ($\approx 3\lambda$) spacing in the NS arm resulting in grating response at intervals of $\Delta m = \pm\frac{\lambda}{6}$ along declination. A source at a zenith angle (za_o) will have its aliased images made for any given allocation at zenith angles za_a given by,

$$sin(za_a) = sin(za_o) + p\frac{\lambda}{6} \tag{5.10}$$

where p is a real integer and λ is the wavelength. The number of aliased images seen for a source (can be six at the maximum in the entire sky in the declination range from -90° to +90°) within the declination range of a delay zone depends upon the actual position of the source in declination (or zenith angle za_o) and the declination range covered by the image. Fig. 5.14(f) shows peaks at the expected declination of three aliased images along with the peak at the actual position (near declination -46.°4) of the source MRC1932-464. Fig. 5.14(f) is inspected to ascertain that the strong sources and their aliased images are

present in each day's image at the expected positions.

Noise in each day's image :

The rms noise is measured in different allocation's images and compared with each other as shown in Fig. 5.14(j). Images with relatively high rms noise (more than 2.5 times compared to the one day images of other nearby allocations) are rejected.

Integrated intensity profile :

At each RA pixel the intensity in the declination range of interest is integrated. This gives a single 1-D series of integrated intensity as a function of RA as shown in Fig. 5.14(n). The integrated profile is used to detect features such as low level interference which affect across the entire declination range at a given RA but have lesser strength than the threshold used during RFI mitigation. With sufficient experience, comparing the 1-D profiles along RA of different images, such cases of low level interference can be identified. In addition the level shifts can also be easily detected in this profile. Images with unusual behavior if any, of the integrated profile are carefully examined and on a case to case basis, a decision is made after required investigation.

Grey scale and color images :

In order to get an overall feel of the general features of each day's image, a grey scale and a color image for the entire region of the sky covered are also displayed. They are visually inspected to check for any unusual sources like transients, satellites and the Sun in the grating lobes (See Fig. 3.2). On average we had to reject about 3% of the images due to such cases.

Artifacts and spurious features :

The individual one day images are also affected by artifacts which have non-astronomical origin. It includes residual DC[6] varying with declination, but constant in RA and most likely to be due to correlator offsets. Fig. 5.14(k) shows a 1-D profile of the residual DC as a function of declination and its Fourier transform is shown in Fig. 5.14(m) for a one day's image. The green line shows the rms noise level in Fig. 5.14(k). We notice from these plots that most of the residual DC is due to short spatial frequencies. At the level of each day's image we allow the residual DC to pass through and their estimation and removal is carried out at the level of full resolution dirty images as discussed in Sec. 5.5.1. At this stage we reject only those images in which the magnitude of this residual DC (obtained at each declination by averaging all points along RA which have intensity magnitude less than 5σ) is unusually high ($>2.5\sigma$) or it varies with sidereal time (due to level shifts).

The bandwidth decorrelation is different in different allocation's image. Due to this

[6]These are ridge like structures in the images which are parallel to constant declination lines (and have constant strength at different RAs), but vary with declination. In each allocation's image these artifacts appear like sinusoidal ripples along declination and are most likely due to correlator offsets.

the full resolution image for a given declination range is obtained by choosing the image made with the appropriate delay setting depending upon the declination range of interest for each allocation in order to minimise the net bandwidth decorrelation.

5.4.3 Bandwidth decorrelation

Each allocation's image suffers different bandwidth decorrelation at different positions along the NS direction. At MRT we use a bandwidth of 1 MHz. As described earlier in Sec. 1.5.3, to reduce the effect of bandwidth decorrelation, the visibilities were observed with a maximum of four different delay settings. For each delay setting we can observe a part of the sky in declination with little decorrelation (maximum decorrelation <20%) around the declination for which the geometrical delay has been compensated. This is referred to as delay zone. The correlation response around the point for which the geometric delay has been compensated is graded by $sinc(\Delta\nu\Delta\tau)$ where $\Delta\nu$ is the bandwidth and $\Delta\tau$ is the uncompensated delay at the declination concerned[7]. The uncompensated delay is given by $\Delta\tau = \frac{y\lambda}{c}\{sin(za_o) - sin(za)\}$, where za_o is the zenith angle for which the geometric delay has been compensated, za is the zenith angle at which we wish to compute the correlation response and y is the baseline length along the NS. So the grading function or the delay beam can also be written as $sinc\{\Delta\nu(\frac{y\,\lambda\,sin(za_o)}{c} - \frac{y\,\lambda\,sin(za)}{c})\}$.

The East arm and the West arm have different cable lengths due to which the baselines formed by E×NS and W×NS suffer different bandwidth decorrelations. To calculate the net correlation response in an image of a given allocation at any declination, we compute the average correlation response due to all the baselines at the concerned declination. The delay settings are same at the level of each block. Since the length of the baselines do not change from one allocation to another significantly in the same block, the correlation response is approximately same. In view of this at the level of a block, the images obtained with the same delay settings are combined together.

For block-1 and block-2 there is only one delay setting, for block-3 there are 2 delay settings, for block-4 there are three delay settings and from block-5 to block-10 four delay settings are used to measure the visibilities. To minimize the net bandwidth decorrelation in the full resolution image, we have made four sets of images by combining images of block-1 and block-2 with different delay zones in block-3 to block-10 as given in Table 5.2. Each set is appropriate to maximize the correlation response for ≈15°-20°declination range.

Fig. 5.17, shows the correlation response for the four sets of full resolution dirty images made after co-adding images of all the allocations from block-1 to block-10. The correlation response for the baselines formed by the East groups with all the NS groups (as dotted

[7] $sinc(\theta) = \frac{sin(\pi\theta)}{\pi\theta}$

Block Number	Different delay zone images of each block co-added to cover entire declination range in the full resolution image			
	I	II	III	IV
1	1	1	1	1
2	1	1	1	1
3	1	1	2	2
4	1	2	3	3
5	1	2	3	4
6	1	2	3	4
7	1	2	3	4
8	1	2	3	4
9	1	2	3	4
10	1	2	3	4

Table 5.2: The table shows different delay zone images corresponding to each block which are combined to obtain the full resolution dirty images in four sets (I, II, III, IV) to cover the entire declination range of MRT with minimum bandwidth decorrelation.

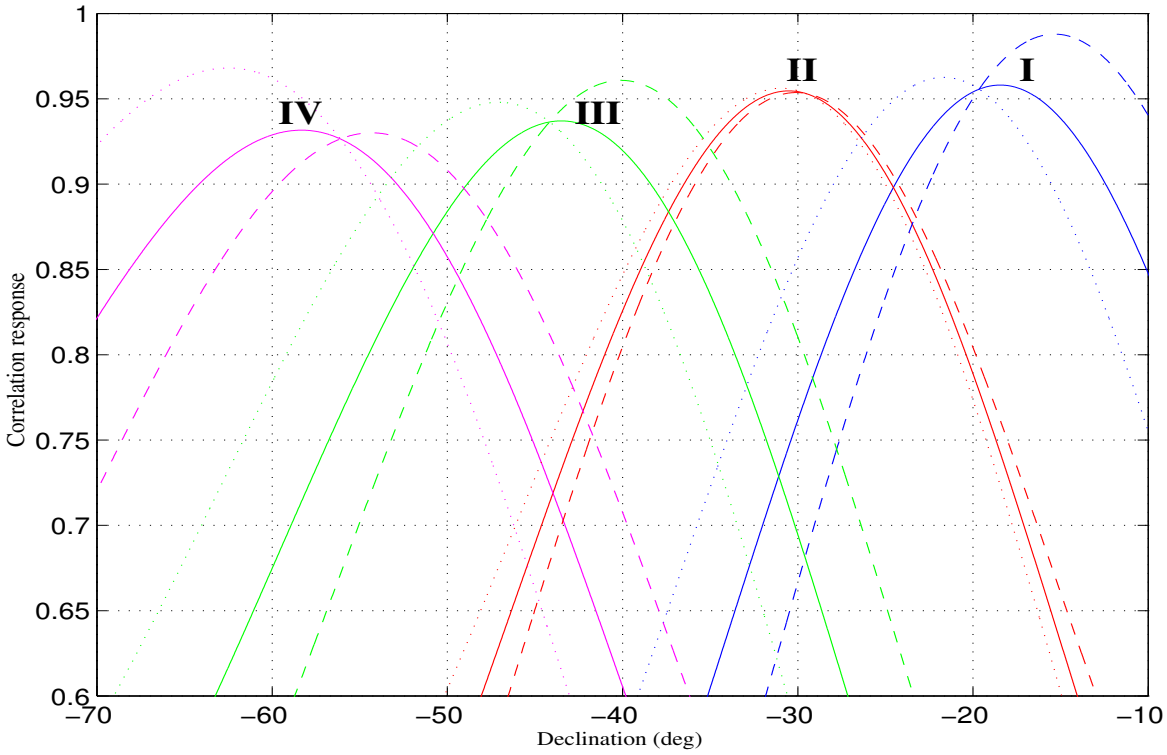

Fig. 5.17: Average correlation response for the four sets of full resolution dirty images made by combining images of all the allocations. The dotted line is for the baselines formed by the East groups with the NS groups, dashed line is for the baselines formed by the West groups with the NS groups and the solid line is for all the baselines. The four sets of images marked as I, II, III and IV are explained in Table 5.2 and Table 5.3. The maximum bandwidth decorrelation expected in the full resolution image is ≈18% at δ=-70°.

Image set number	Declination Range	Correlation response maximum	minimum
I	-10° to -25°	0.96	0.85
II	-25° to -37°	0.96	0.88
III	-37° to -52°	0.94	0.87
IV	-52° to -70°	0.93	0.82

Table 5.3: The table shows the declination range corresponding to each of the four sets of full resolution images obtained to minimize the net bandwidth decorrelation across the entire declination range. The maximum and the minimum correlation response within each declination range covered is also shown.

lines) and the West group with all the NS groups (as dashed lines) are separately shown. The net correlation response which is the average of these two is shown by a solid line. The declination range considered for each delay zone and the maximum and minimum correlation response within each delay zone is also shown in Table 5.3. The maximum bandwidth decorrelation is $\approx$ 18% at δ=-70°. The maximum correlation response for different baselines is at slightly different declinations (as the delays can only be changed in units of 0.376μs). Due to this the maximum correlation response in the image is less than unity.

From the correlation curves we can draw a few straightforward inferences. We note that the peak of the correlation curves for the baseline formed by the East arm with the NS trolleys and the West arm with the NS trolleys do not coincide at the same declination due to different lengths of the cable. The delays used are in steps of 0.376 μs (corresponding to the sampling frequency of 2.65625 MHz), while in principle the delays in steps of 0.0834 μs (corresponding to the sampling frequency of 12 MHz) could have been used . This would have given more flexibility in fixing the delay centers accurately. Unfortunately, this aspect was left out in the design of the recirculator.

The net effect of bandwidth decorrelation on the determination of the relative weights for co-addition of each allocation's image and the resulting full resolution dirty image has been incorporated in the estimation of PSF used for deconvolution which is discussed in Sec. 6.3.2.2. Each day's image has to be co-added using appropriate relative gains to obtain the full resolution images which is discussed below.

5.4.4 Estimation of relative weights to add each day's image

Once each day's image is checked for its quality the next step is to suitably combine them to obtain the full resolution dirty image. There are several ways to combine the images and the most suitable way depends upon the application in mind. Our aim is to obtain the beam closest to a *sinc* function for which we need to add the images in such a way that all

Source Name MRC	RA (J2000)	Declination (J2000)	Flux density (Jy) (408 MHz)	(150 MHz)
1618-430	16:22:03.1	-43:08:16	6.5	15
1754-597	17:59:06.2	-59:46:56	12.6	21
1827-360	18:30:59.0	-36:02:35	25.8	31
1932-464	19:35:57.1	-46:20:44	39.6	91
2032-350	20:35:47.6	-34:54:04	17.6	33
2140-434	21:43:33.4	-43:12:48	9.2	21
2211-172	22:14:25.6	-17:01:44	28.7	84
2331-416	23:34:26.1	-41:25:19	15.9	34

Table 5.4: The sources used to estimate the relative gains in each day's image used for co-addition.

the spatial frequencies covered should get equal weight.

At MRT first all individual images of the same allocation are combined with natural weights (square of the signal to noise ratio, after equating the deflections obtained on the same source) and one resultant image with the maximum possible signal to noise ratio is obtained for each allocation. The resulting images obtained for each allocation were combined (across different allocations) with weights equal to inverse of deflection to obtain the full resolution dirty image. This hybrid approach achieves the best possible sensitivity with the constraints of obtaining dirty beam closest to a *sinc* function. Since the *uv* coverage is nearly complete and uniform, the PSF is essentially of a filled cross. The weights used while co-adding images for all the four delay zones are derived via fitting for the images of the delay zone in which the strongest unresolved source is present and applied to the images of all the delay zones. Table 5.4 gives a list of sources and their positions which were used to estimate the relative gains in each sidereal hour image.

For each sidereal hour range, four sets of full resolution dirty images are produced separately to cover the entire declination range of MRT. The full resolution dirty images are also affected by spurious features which are of non-astronomical origin. We now describe the likely reasons and discuss their removal from the images.

5.5 Artifacts in images

The artifacts in the full resolution images are mainly due to correlator offsets and aliased images. These are discussed below.

5.5.1 Correlator offsets

On visual inspection of the full resolution dirty images we noticed ridge like structures in the images which are parallel to RA axis. Their strength is constant with time (i.e. RA) but varies with declination (See Fig. 5.18). These artifacts appear like sinusoidal ripples along

declination and are likely due to correlator offsets, which are almost constant in time. In general the correlator offsets are usually negligible unless either the correlator is malfunctioning or there is a significant cross talk between various antennae. If the variations are short term they may act like stochastic noise which may average out to some extent. These offsets are generally low in most of the correlator channels. However, one or two correlator channels may have higher positive or negative offsets. These look like delta functions and when Fourier transformed appear as a sinusoid. However, most of the sinusoid remains buried in the noise except when their intensity is higher than the noise. Being constant in time they appear as parallel lines along RA in the images. They could also be due to sidelobes of circumpolar sources (Golap, 1998). Field tests indicate these correlated, spurious signals do not seem to originate from the electronics of the laboratory or the field.

Correlator offsets in the images with partial resolution :

The images of the survey with partial resolution (Golap, 1998) were also affected by correlator offsets. To remove these offsets the following procedure was used. The correlator output for 24 hours is considered. The interference points in the visibilities are rejected and interpolated from data at adjacent times. A Fourier transform was performed on the whole stretch of the visibility data. In the Fourier domain, the zero frequency component was cut off and an inverse Fourier transform was performed to get back the visibilities without the correlator offsets. The rejection of the zero frequency component is equivalent to bringing back to zero the net power output from a correlation telescope. The fringes are sampled at 0.9130 point per sidereal second which corresponds to 78888 points in 24 hours (data from first cycle was used to synthesize the images). So in each visibilities the fringe frequencies up to 1.2×10^{-5} Hz was filtered. This corresponds to the contribution by point sources below -88°in declination and also by broad structures larger than 60°in size. Since mapping such broad features was not the objective, the removal of correlator offsets therefore, did not adversely affect the true intensity distribution in the images.

Removal of correlator offsets in full resolution image :

To remove the effect of correlator offsets from the full resolution images, the most appropriate thing would have been to follow the prescription similar to the one employed in the survey with partial resolution. But in practice applying the same approach is impractical due to the following reasons. For the survey with partial resolution only those observations which were uninterrupted for one complete day, were used. In the case of full resolution image uninterrupted observations for one complete day are not available for the data used on most of the day's which makes the same approach infeasible. In addition such an approach is computationally expensive and would be difficult to implement since the full resolution images have been synthesized using a large number of day's of

data for four different delay zones. So we needed to come up with a method to estimate and remove the residual DC from the full resolution dirty image itself before deconvolution. It is important to do so, since deconvolution being a nonlinear process can behave adversely in presence of this residual DC varying along declination.

Strength of residual DC :

The full resolution dirty image was first convolved along RA with a *sinc* function of FWHM 16 s which is the expected beam width at δ=0°, in order to increase the signal to noise ratio. To get a rough estimate of the problem the following analysis was carried out. Since the DC is constant with RA, an estimate of its strength was made by taking the average of the one dimensional cut along RA at each declination. The estimation of the residual DC gets adversely affected due to rms noise and the presence of astronomical signal. The effect of rms noise can be suppressed by including a large number of samples along RA at any declination. To reduce the effect of astronomical signal we considered only those points for DC estimation which had strength within $\pm 3\sigma$. If we assume the noise to be Gaussian[8] $\approx$99% of the points which do not have significant level of astronomical signal would still be included in the DC estimation. There are a few regions in the sky where due to sidelobes along RA of strong sources, we were not able to estimate this DC accurately. In such a scenario whenever the total number of points available for DC estimation at any declination, were less than half the total number of points along RA in the image, the DC was estimated by interpolating the DC at adjacent declinations. A one dimensional profile of the residual DC along declination in the image is obtained as a result of this exercise.

The investigation of the various residual DC profiles revealed that the residual DC is of the order of rms noise in the image (generally varies between -σ to +σ) and the maximum value always lies within $\pm 2\sigma$. The Fourier transform of the 1-D profiles revealed that most of the residual DC is due to short spatial frequencies[9].

DC overestimation due to strong sources :

The DC is subtracted from the original image and an example of the re-estimated DC remaining in the resultant image is shown in Fig. 5.19(a) along with its Fourier transform in Fig. 5.19(b). Although the remaining DC is generally much lesser than the rms noise, we also note that the DC removed was overestimated which is evident from residual DC

[8]This is not strictly true in presence of astronomical signal, but gives a rough idea of how many genuine points not affected by astronomical signal would be included.

[9]In order to investigate the possibility of obtaining full resolution images free from any residual DC (within acceptable levels), we also obtained the full resolution dirty image by combining images only from allocations 13 to 63 (excluding allocations 1 to 12 i.e. short baselines), which revealed that although the strength of the residual DC in the images was lesser but it still had sufficient strength which cannot be neglected and needs to be removed. Since the residual DC was successfully removed later in the full resolution images, all the allocations were used to obtain the full resolution images presented in this thesis.)

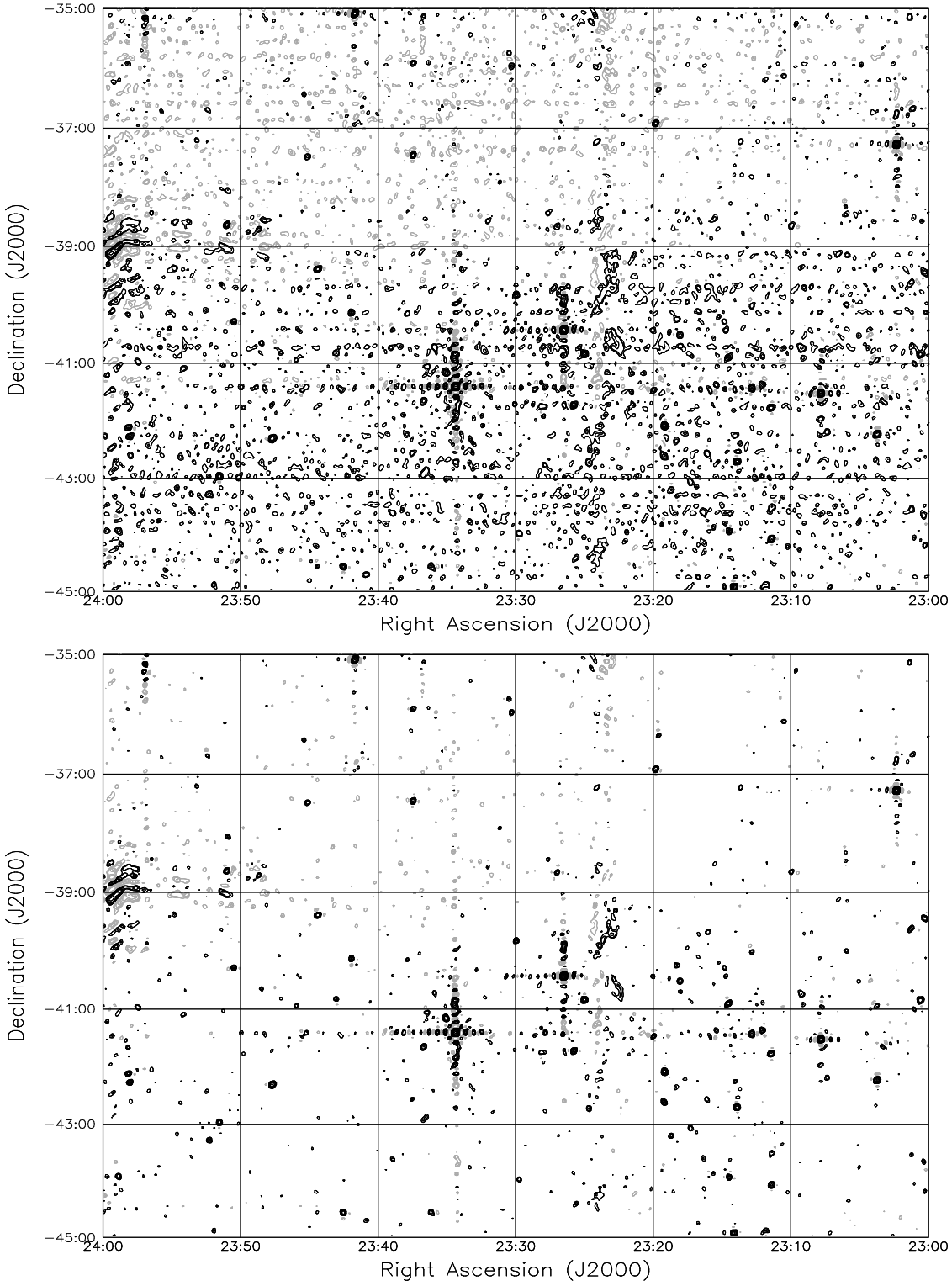

Fig. 5.18: Full resolution dirty image obtained by co-adding images of all the allocations. The upper contour image is the original image before residual DC is removed. The contour image shown in the lower plot is obtained after DC removal has been carried out using the scheme depicted in Fig. 5.20. The contour levels are -10, -7, -5, -3, -2, 2, 3, 5, 7, 10, 14, 20, 28, 40, 60$\times\sigma$ where σ is the rms noise in the image. The image intensity is in arbitrary units. The DC still present in the image shown in the lower plot is within ±20% of the rms noise. This is a specific case of an image severely affected by residual DC.

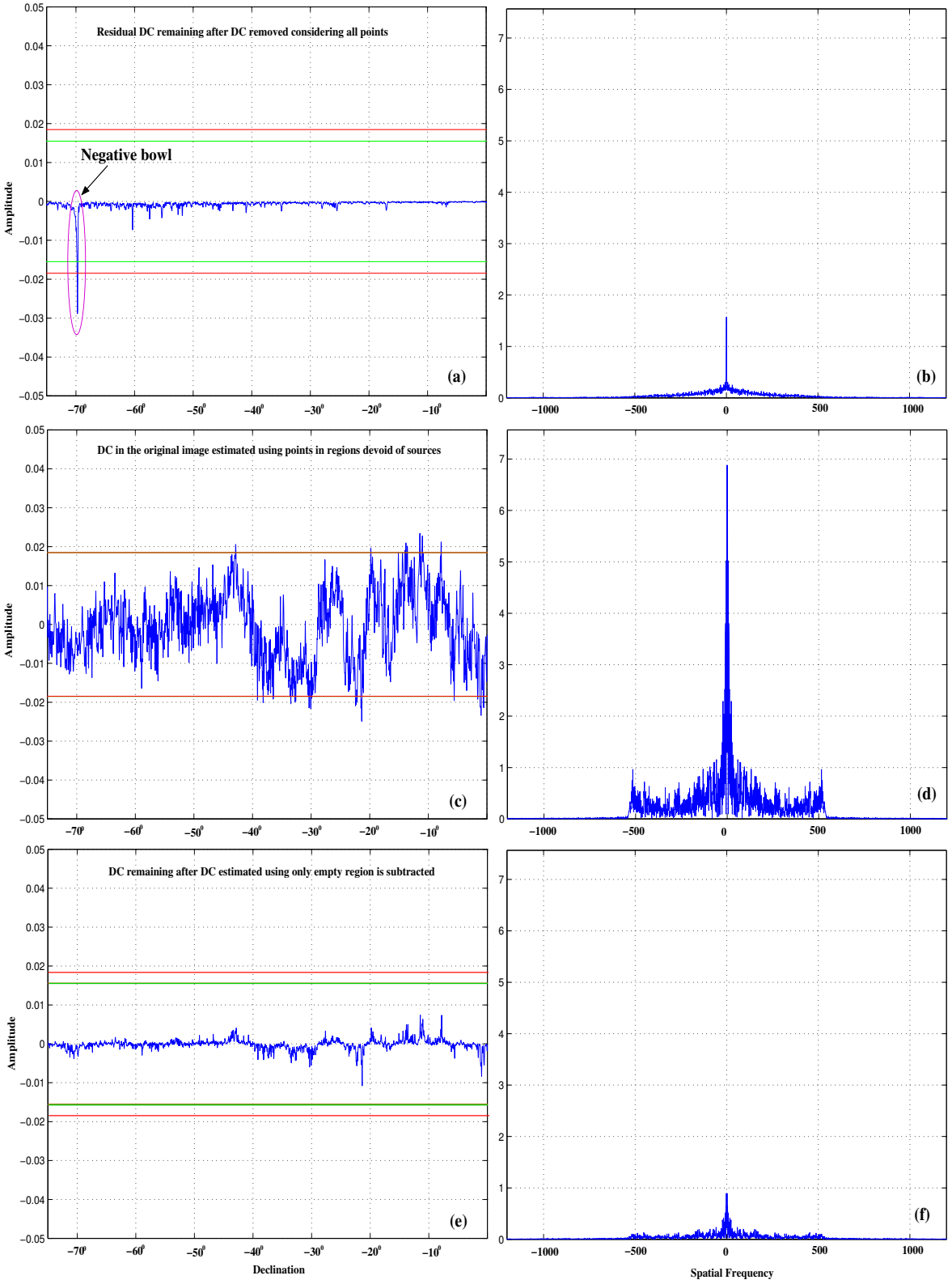

Fig. 5.19: The plots show the residual DC as a function of declination (left column) and its Fourier transform as a function of spatial frequency (right column) in the full resolution images obtained by adding all the allocations before and after DC removal (See Sec. 5.5). The scale on the y-axis in all the subplots are in arbitrary units. The red lines indicate the rms level (1σ) before DC removal and the green line indicates rms level (1σ) after DC removal.

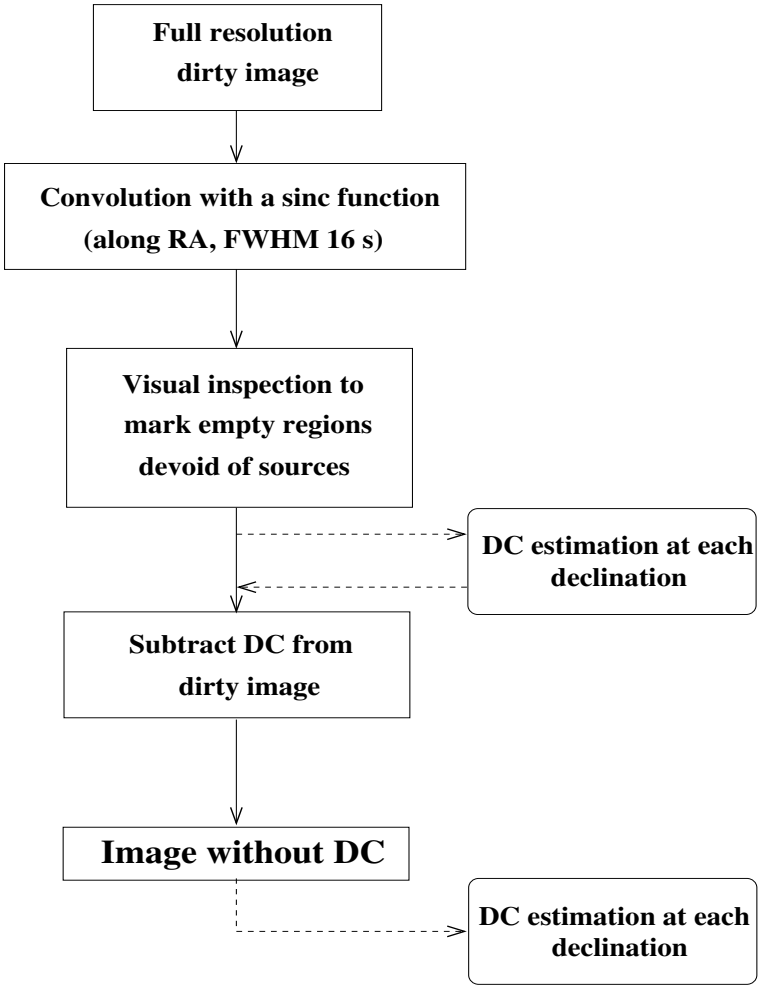

Fig. 5.20: Flow chart to estimate and remove the residual DC from the full resolution images using only empty regions.

remaining being negative at all declinations[10]. This is due to the effect of astronomical signal on the DC estimation which is essentially positive in the original image and hence biases the DC estimation towards positive value. This effect is more pronounced at declinations where there are strong sources (whose sidelobes along RA affect DC estimation very significantly) and can be easily noted in Fig. 5.19(a), which shows an abrupt negative bowl of strength $\approx 2\sigma$ created in the image due to DC removal near the declination -69.°7 which is the declination position of two strong sources in the image, namely MRC2152-699(RA 21h:57m:06.6s, declination -69°41′33″; 58 Jy at 408 MHz and 102 Jy at 151.5 MHz) and MRC2153-699(21h:57m:43.9s, -69°41′51″; 21 Jy at 408 MHz and 34 Jy at 151.5 MHz).

[10]In an effort to investigate the possibility of improvement in the DC estimation we also applied a moving box-car average (with various window widths) on the 1-D profile of the residual DC in the original dirty image, assuming that the DC varies slowly with declination. We expected that the moving box-car average would improve the DC estimation due to substantial increase in the number of samples. But box-car averaging did not result in any improvement in DC estimation.

Suppression of astronomical signal to improve DC removal :

In order to further suppress the DC overestimation due to the presence of astronomical signal, we adopted the scheme shown in Fig. 5.20. A contour and grey scale image of each full resolution image is visually inspected and all such regions which are devoid of sources are manually marked. At any declination only those pixels along RA which lie in these empty regions are considered for DC estimation[11]. Due to this the number of RA points available to estimate the residual DC were significantly reduced. Since we also image guard zones extending to about 54 minutes in RA on both the sides of sidereal hour range of interest we still have at least 900 points at any declination within these marked empty regions. Fig. 5.21 shows the number of RA points at different declinations available in such marked empty regions for the full resolution images for each of the four delay zones corresponding to images for different sidereal hour ranges.

Fig. 5.19(c) shows the DC estimated as a function of declination in the original image and Fig. 5.19(d) shows its corresponding Fourier transform as a function of spatial frequency. The DC is subtracted from the original image and the re-estimated DC in the resultant image after DC subtraction is shown in Fig. 5.19(e) along with its Fourier transform in Fig. 5.19(f). It is clear from the Fig. 5.19(e) that there is no significant effect of astronomical signal on the DC estimation since the residual DC still remaining after first iteration shows noise like characteristics with nearly zero mean and there is no negative bowl created due to DC removal at declination at which strong sources are present in the image. With this approach even in the images which contain the Galactic plane, the DC could be estimated and removed satisfactorily. Fig. 5.18 shows a part of the full resolution dirty image severely affected by residual DC and after DC removal by this approach. It is clear the the DC removal is very satisfactory. For all the images presented in this dissertation, DC removal was carried out using this approach.

Effect of DC removal on the image :

It is important to ascertain the effect of DC removal on the images. We have used only regions which are devoid of any significant astronomical signal to estimate the DC. In addition only those pixels whose strength is within $\pm 3\sigma$ have been used which further reduces the contribution even from weaker sources in these empty regions. The value of this original DC affecting the images is of the order of rms noise in the image. The number of independent samples along RA at any declination at least span one sidereal hour range which heavily suppresses the effect of rms noise on the DC estimation and sidelobes of weaker sources. Thus any modification of the actual sky due to error in this DC estimation is expected to be insignificant compared to the rms noise present in the images.

[11] We recall that DC estimation is always carried out using only those pixels whose strength is within $\pm 3\sigma$.

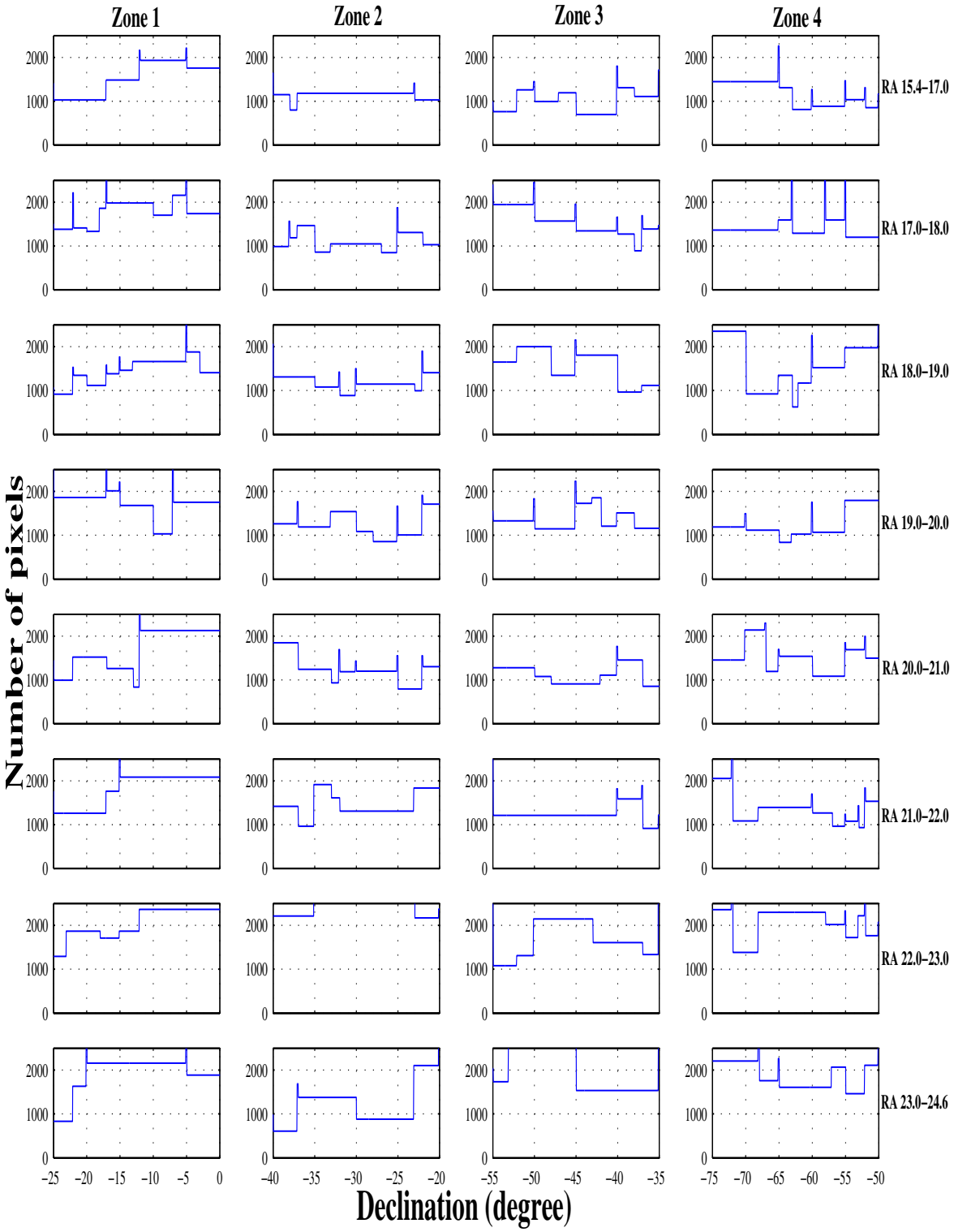

Fig. 5.21: The plots show the number of pixels available at different declinations for estimation of DC in the regions which are visually marked as devoid of significant astronomical signal (empty regions) for all the four delay zones of full resolution dirty images corresponding to each sidereal hour range. The plots clearly reveal that there are sufficient number of independent pixels (at least 900) at any declination in the empty regions so as the effect of rms noise and astronomical signal on the DC estimation can be heavily suppressed. The scales on the x-axis and the y-axis in all the subplots within each column are same. The maximum number of pixels shown on the y-axis in all the subplots is 2500.

We also verified this by visually inspecting the images produced with and without the residual DC removed. Careful inspection and analysis did not reveal any perceptible effect on the real features. Further, to re-confirm, we checked for any remaining DC in the residuals after deconvolution and found no significant DC was present, indicating the DC removal at the dirty image stage itself is satisfactory. The DC still present in the final images is low and always less than one fifth of the rms noise.

5.5.2 Grating response/Aliased images

The dirty images were also affected by spurious features due to strong sources in the northern sky appearing in grating lobes and aliased images of a few strong sources which are present in the field of view. These appear due to a few missing allocations and due to the relative gains used to combine the one day images. The relative gains in each day's image is estimated by taking the inverse of the deflection obtained on a common source so as to combine them with uniform weights. Unfortunately the bandwidth decorrelation at any given declination in the images of different allocations is different which results in non-uniform weights. Normally in an image made by combining all the allocations within a given block, the aliased images get cancelled out if the weights are perfectly uniform. Since that is not the case and in addition there are a few missing allocations, aliased images do not get cancelled out completely. For strong sources their effect can be significant. Generally such images can easily be identified by their extended fuzzy appearance and occurrence at the same RA as of the actual source at the expected declinations. Fig. 5.22 shows an example of Cygnus A appearing as grating lobe in the full resolution dirty images and corrupting the entire declination range near RA 20 hrs. Such regions are masked and not considered for any astronomical interpretation. These aliased images also contribute to the rms noise in the images.

5.6 4′×4.′6 Dirty images

We synthesized the full resolution images covering the RA range 15h06m to 24h54m and declination range -80° to -5° (J2000) up to about 3 dB points of the primary beam with angular resolution of $4'\times4.'6\sec(\delta+20.^\circ14)$. For each sidereal hour range images were obtained along with guard zones on both sides in RA (covering ≈54 min on each side). The full declination range is covered by a set of four images obtained to minimize the bandwidth decorrelation. A preliminary analysis is carried out to check for any artifacts, rms noise and confirm presence of strong sources at the expected positions. Inspection and analysis of the final images revealed that they are free from any perceivable interference.

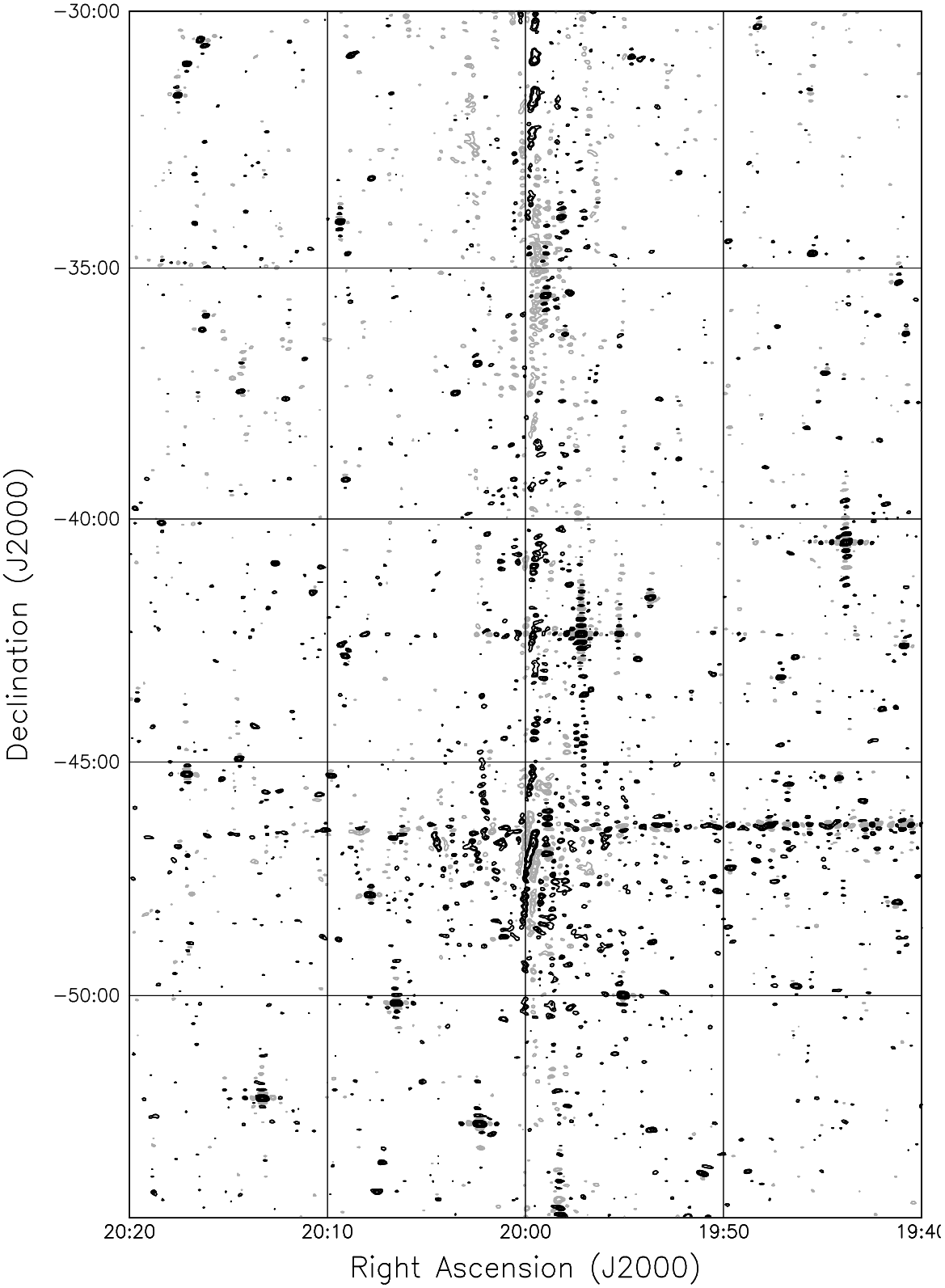

Fig. 5.22: A contour representation of the full resolution dirty image affected by Cygnus A appearing in grating lobes around RA 19.58 hr and across the entire declination range shown. The corrupted regions are not considered for any astronomical interpretation. The contour levels are -7, -5, -3, 3, 5, 7, 10, 14, 20, 28, 40, 60, 100×σ where σ is the rms noise in the image. The image intensity is in arbitrary units.

Artifacts in form of residual DC varying with declination and constant along RA have been estimated and appropriately removed. Fig. 5.23 shows a full resolution dirty image. The dirty images were also analysed by cross comparing them with Culgoora and MRC catalogues. Here we skip those aspects of analysis which are again carried out at the level of deconvolved images (discussed in Chapter 7). The dirty images need to be deconvolved for further analysis. The deconvolution of these wide field images is discussed in the next chapter.

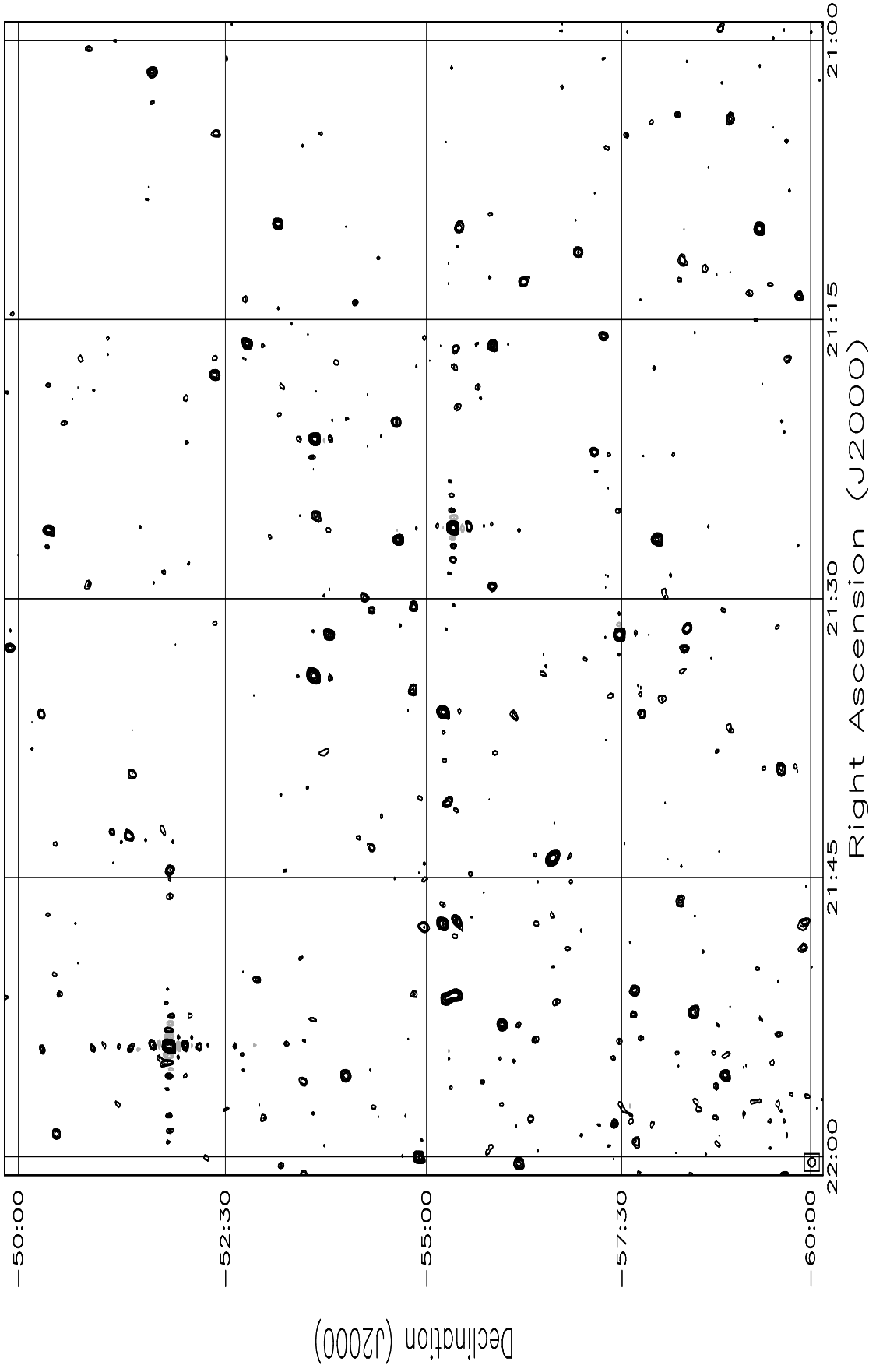

Fig. 5.23: An contour image showing the dirty map covering the RA range 21 hrs to 22 hrs and declination range -60°to -50 °. The contour levels are -7, -5, -3, 3, 5, 7, 10, 14, 20, 28, 40, 60, 100×σ where σ is the rms noise in the image. The image intensity is in arbitrary units.